PHYSICAL REVIEW A **87**, 043410 (2013)

Trapping ions from a fast beam in a radio-frequency ion trap: Exploring the energy exchange with the longitudinal radio-frequency field

Annette Svendsen, Lutz Lammich, John E. Andersen, Henrik K. Bechtold, Erik Søndergaard,
Frank Mikkelsen, and Henrik B. Pedersen
Department of Physics and Astronomy, Aarhus University, DK-8000 Aarhus C, Denmark

(Received 20 March 2013; published 12 April 2013)

The possibility of injecting ions from an initially fast moving beam into a multipole radio-frequency (RF) ion trap without the use of buffer gas is described. The chosen trap geometry gives rise to an oscillating electric field along the direction of the incoming ions, and through an analytical model as well as numerical simulations it is demonstrated that the energy exchange between the injected ions and this oscillating field governs the trapping dynamics. Most notably, if ions arrive at the trap during specific phases of the RF field, they can be effectively decelerated and stored with low kinetic energy even if their kinetic energy initially exceeds the depth of the trapping potential well. An experimental apparatus for trapping ions from a fast beam is described, and experimental investigations demonstrating the described trapping dynamics are presented.

DOI: 10.1103/PhysRevA.87.043410 PACS number(s): 37.10.Ty

I. INTRODUCTION

The development and characterization of ion traps has been essential to several modern experiments seeking to understand the most basic properties of atoms and molecules on the quantum level. These investigations often entail preparing systems in well-defined quantum states which are subsequently manipulated, an approach that relies heavily on the ability to trap the studied species over long time.

Since the introduction of ion traps in the 1950s [1], the field of ion trapping has developed strongly, and the scientific scopes of today's ion trapping experiments are very diverse, including, for instance, studies of strong interactions between single ions and photons in cavity QED [2,3] and of quantum logic and coherent control [4], studies of cold chemistry with either single ions or ensembles of ions [5–7], as well as spectroscopy of small molecular ions [8] and of large biomolecular ions [9–12]. Most studies represent in-trap experiments, but ion traps are also frequently used for storage and accumulation of ions between injections into other experimental setups like storage rings [13,14], other ion traps [15], or photoelectron spectrometers [16].

Several experiments use the radio-frequency (RF) quadrupole ion trap devised by Paul *et al.* [1,17]. The special field geometry of this trap allows for an analytical description of the ion motion and furthermore offers the advantage of in-trap mass analysis of the stored species [18]. A disadvantage of the Paul trap is the extension of the confining RF field over most of the trapping volume implying that the ion micromotion driven by the time-varying field is significant except very close to the trap center. This effect becomes problematic for experiments striving to obtain internally cold molecular ions [19,20] by letting trapped ions collide with a cold buffer gas. In these cases, the combination of the RF-driven micromotion and the ion-gas collisions leads to heating of both the external and the internal degrees of freedom of the trapped ions [19,20]. This effect can be avoided with higher-order multipole traps as pioneered by Gerlich [21]. In such traps, the micromotion is strongly suppressed, and ions can hence be cooled both translationally and internally to temperatures of ∼10 K with the sacrifice of the mass-selectivity and the analytical description of the ion motion [19].

A central issue in experiments with RF traps is the method of loading ions into the trap. Ions can be created inside the trap volume by electron impact or chemical- or laser-induced ionization of the background gas. Evidently, only a limited number of ionic species can be created in this manner and thus more universal methods of injecting ions generated by external ion sources have been developed [22]. One approach is to inject ions into the trap in the presence of a He buffer gas which dissipates the ion kinetic energy through collisions. This method is used extensively, e.g., in the case of multipole traps and requires He densities of the order of 10^{14} cm^{-3} [$\sim$6–400 $\times$ 10^{-5} mbar depending on temperature (4 K–300 K)] to dissipate enough kinetic energy on the required time scale. Advantageously, collisions with the He buffer gas can bring the ion internal degrees of freedom into thermal equilibrium with the buffer gas, and by controlling the temperature of the trap specific internal temperatures of the ions can thus be achieved. The presence of the buffer gas might also lead to disturbing effects: If ions are to be extracted from the trap and injected into another part of the experimental setup for further studies, collisions with He during the extraction phase can lead to heating. The buffer gas may be pumped away before extraction, but this is usually a slow process since the gas density has to change by several orders of magnitude [23]. Experiments can be performed inside the trap, but this rules out the detection of neutral fragments and electrons emerging from, for example, photoexcitation or -ionization experiments. Furthermore, dynamical information, like the kinetic energy released in the fragmentation process, is lost during trapping due to collisions between the buffer gas and the fragments. Finally, the fragmentation process itself or fluorescence might be quenched due to the removal of internal energy in the interaction with the buffer gas.

In this paper, the possibility of injecting ions from an initially fast moving beam into a multipole RF trap without the use of buffer gas is explored. The chosen trap geometry gives rise to a component of the confining RF field along the direction of the injected ions, and the energy exchange between the ions and this longitudinal field component facilitates stable trapping of low-energy ions though their kinetic energy initially exceeds the depth of the trapping potential. In Sec. II, the description of ion trapping within the adiabatic approximation is summarized, and an expression for the depth of the trapping potential is derived for the chosen trap geometry. In Sec. III, a formulation to describe the trapping mediated by the longitudinal field is developed, and the introduction of a few approximations results in a simple analytical expression that describes the dependance of ion trapping on relevant parameters like the kinetic energy of the incoming ions and the RF amplitude. The trapping mechanism emerging from the model is demonstrated, and in Sec. IV it is validated through comparison with numerical simulations. Furthermore, the influence of the longitudinal field on the properties of the trapped ions, i.e., in particular the final ion kinetic energy, is illustrated and discussed on the basis of the presented model and simulations.

An experimental setup to trap ions from a fast-moving beam is described in detail in Sec. V, and an experimental investigation of the described injection mechanism and properties of the trapped ions is presented in Sec. VI. In Sec. VII, the findings are discussed and compared to previous studies.

II. ADIABATIC ION TRAPPING IN RADIO-FREQUENCY FIELDS

A. Adiabatic ion motion in RF fields

The equation of motion of an ion in an RF field is

$$m\ddot{\vec{u}} = qe\vec{E}_0(\vec{u})\cos(\omega t), \tag{1}$$

where $\vec{u}$ is the ion position, m and qe the ion mass and charge, respectively, $\vec{E}_0(\vec{u})$ the electric field amplitude at the ion position, and ω the angular frequency of the time-varying electric field. In general, this equation cannot be solved analytically. In the adiabatic approximation [19,24], the ion motion is assumed to separate into a rapidly oscillating component, $\vec{\xi}(t)$, the so-called *micromotion* following the RF field, and a slower *drift* motion, $\vec{R}(t)$, implying that the ion position can be written as

$$\vec{u}(t) = \vec{R}(t) + \vec{\xi}(t). \tag{2}$$

By further assuming that the electric field amplitude only varies slightly over the distance traveled by the ion during one period of the micromotion, the following equation of motion for the drift coordinate is obtained [19]:

$$m\ddot{\vec{R}}(t) = -\vec{\nabla}U_{\text{eff}}(\vec{R}), \tag{3}$$

where the effective potential, U_{eff}, is given by

$$U_{\text{eff}}(\vec{R}) = \frac{q^2e^2}{4m\omega^2}|\vec{E}_0(\vec{R})|^2. \tag{4}$$

The equation for the drift motion [Eq. (3)] describes the ion motion under a time-averaged force which originates from the inhomogeneity of the electric field. In particular, the time-averaged force is conservative as it can be expressed as the gradient of a potential energy function [Eq. (4)] which can be shown [19] to represent the time-averaged kinetic energy stored in the micromotion. Thus, these equations imply that the time-average of the ion energy is a constant of motion. If, however, the electric field amplitude experienced by the ion changes significantly during one period of the micromotion, the adiabatic approximation breaks down and the electric field can exchange energy with the ion. The regime within which the adiabatic approximation remains valid can be quantified through the adiabaticity parameter given as [19]

$$\eta = \frac{2|qe\vec{\nabla}|\vec{E}_0||}{m\omega^2}. \tag{5}$$

For the adiabatic approximation to hold and for ion motion to be stable, simulations reveal that η must fulfill the requirement $\eta < \eta_{\text{max}} = 0.30$ [19], whereas recent experiments suggest that $\eta < 0.36$ is sufficient [25].

To achieve trapping of an ion at rest, a potential well must be created. This is not possible using purely electrostatic fields because ion motion in this case is governed by the electric potential which does not exhibit local minima or maxima as a direct consequence of Laplace's equation [26]. As discussed above, ion motion in RF fields is governed by the effective potential [Eq. (4)], which in general can have local minima since it depends only on the magnitude of the electric field and not on its direction. Consequently, ions can be trapped in RF fields by choosing appropriate field geometries.

B. The ring electrode trap

A special realization of an RF ion trap is the ring electrode trap [19]. This trap consists of a series of coaxial ring electrodes as shown in Fig. 1(a). To trap ions in the radial direction, RF potentials of opposite phase, $\pm V_0\cos(\omega t)$, are applied to the ring electrodes in an alternating fashion. For the ideal configuration satisfying the boundary condition $V(\hat{r}_0,\hat{z}) = V_0\cos\hat{z}$, the electric field amplitude is given by [19]

$$\vec{E}_0 = (E_r,E_z) = \frac{V_0}{z_0 I_0(\hat{r}_0)}(-I_1(\hat{r})\cos\hat{z}, I_0(\hat{r})\sin\hat{z}). \tag{6}$$

Here, $2\pi z_0$ is the distance between ring electrodes of the same phase and r_0 the inner radius of the ring electrodes as shown in Fig. 1(a). Furthermore, $\hat{z} = z'/z_0$ and $\hat{r} = r/z_0$ gives the axial and radial position in units of z_0, $\hat{r}_0 = r_0/z_0$ is the reduced inner radius, and I_i the ith modified Bessel function. Inserting Eq. (6) into Eq. (4) yields the following expression for the effective potential:

$$U_{\text{eff}}(\hat{r},\hat{z}) = \frac{q^2e^2V_0^2}{4m\omega^2 z_0^2 I_0^2(\hat{r}_0)}\left[I_1^2(\hat{r})\cos^2(\hat{z}) + I_0^2(\hat{r})\sin^2(\hat{z})\right]. \tag{7}$$

This expression is plotted in Fig. 1(c) for a $\text{Si}_2{}^-$ ion ($m =$ 56 amu) with parameters relevant for the present experimental setup. For this trap geometry, trapping in the axial direction is obtained by applying static electric potentials to electrodes at each end of the ring electrode array (end-cap and lens electrodes). A typical trapping potential along the trap axis created by these end electrodes with the ring electrode array on ground potential is shown in Fig. 1(b). For the ring electrode trap, the adiabaticity parameter [Eq. (5)] can be expressed analytically as

$$\eta(\hat{r},\hat{z}) = \frac{2|q|V_0}{m\omega^2 z_0^2 I_0(\hat{r}_0)}\sqrt{\frac{\left[I_1(\hat{r})I_0(\hat{r}) - I_1^2(\hat{r})\cos^2\hat{z}/\hat{r}\right]^2 + \left[I_0^2(\hat{r}) - I_1^2(\hat{r})\right]^2\cos^2\hat{z}\sin^2\hat{z}}{I_1^2(\hat{r})\cos^2\hat{z} + I_0^2(\hat{r})\sin^2\hat{z}}}. \tag{8}$$

Figure 1(d) displays the adiabaticity parameter for a $\mathrm{Si_2}^-$ ion ($m = 56$ amu) as a function of the radial position at two positions along the trap axis. The graph illustrates that η increases with the radial position, thereby implying that adiabatic ion motion occurs in the interior of the trap volume, where $\eta < 0.3$.

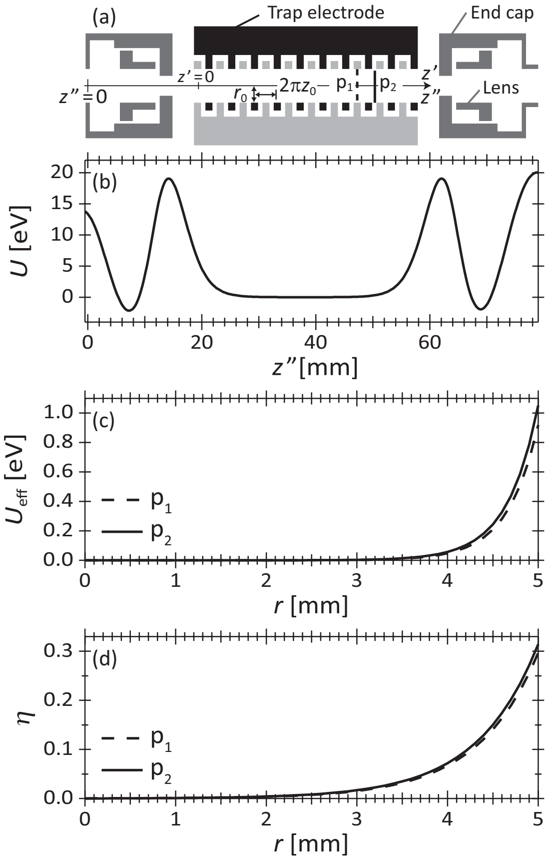

FIG. 1. Characteristics of the ring electrode trap used in this work. (a) Schematic of the ring electrode trap showing the geometrical quantities characteristic for the ring electrode trap, $r_0 = 5$ mm and $2\pi z_0 = 4$ mm. [A three-dimensional (3D) representation of the trap assembly can be see in Fig. 11.] (b) The potential energy of an ion of charge $-1e$ along the center axis of the trap when only static potentials are applied to the end caps and lenses. For the shown configuration, the lens potentials are +10 V while the end-cap potentials are set to −25 V. (c) Effective potential energy [Eq. (7)] in the radial direction for $\mathrm{Si_2}^-$ at an RF amplitude of 25 V with a frequency of $\omega = 2\pi \times 4$ MHz. The solid and dashed lines show the effective potential at the z' positions indicated by the solid and dashed lines in (a). (d) The adiabaticity parameter, η [Eq. (8)], in the radial direction for $\mathrm{Si_2}^-$ at an RF amplitude of 25 V with a frequency of $\omega = 2\pi \times 4$ MHz. The solid and dashed lines show η at the z' positions indicated by the solid and dashed lines in (a).

C. The concept of trap depth

An important property of any trap is the depth of its confining potential, the so-called trap depth. For an RF trap, the trap depth is not necessarily determined only by the effective potential, as ion motion might not be stable in regions of high effective potential due to the breakdown of the adiabatic approximation. For a 22-pole trap, Mikosch *et al.* [25] instead identified the trap depth as the effective potential at the edge of the trapping volume. Thus, for a given RF trap, we define the trapping volume as the volume within which ion motion is stable according to the adiabatic approximation, namely the region where $\eta \leqslant \eta_{\text{max}}$. For the ring electrode trap, η and U_{eff} depend on both the axial and the radial positions, $\hat{z}$ and $\hat{r}$, and the trapping volume is bounded by the $(\hat{r},\hat{z})$-contour line corresponding to $\eta(\hat{r},\hat{z}) = \eta_{\text{max}}$. The trap depth is then the minimum of the effective potential along this line:

$$\text{model 1,}\quad U_{\text{trap}} = \min\{U_{\text{eff}}(\hat{r},\hat{z})\,|\,\eta(\hat{r},\hat{z}) = \eta_{\text{max}}\}. \tag{9}$$

An alternative and simpler approach for the ring electrode trap is to define the trapping volume as the maximum cylindrical volume over which $\eta \leqslant \eta_{\text{max}}$, implying that its radius, $\hat{r}_{\text{max}}$, is the maximum radius at which $\eta(\hat{r}_{\text{max}},\hat{z}) \leqslant \eta_{\text{max}}$ for all $\hat{z}$. The trap depth is then defined as the minimum of $U_{\text{eff}}(\hat{r}_{\text{max}},\hat{z})$ over all $\hat{z}$:

$$\begin{aligned} \text{model 2,}\quad r_{\text{max}} &= \max\{\hat{r}\ |\eta(\hat{r},\hat{z}) \leqslant \eta_{\text{max}}\ \forall\ \hat{z}\}, \\ U_{\text{trap}} &= \min_{\hat{z}} U_{\text{eff}}(\hat{r}_{\text{max}},\hat{z}). \end{aligned} \tag{10}$$

The trapping volume boundary, the effective potential along this boundary, and the trap depth obtained from the two definitions are illustrated in Figs. 2(a) and 2(b). Similar results for the trap depth as a function of the RF amplitude are obtained for the two models, but the latter, model 2, offers the advantage that analytical expressions can be derived for essential quantities. Consequently, only the trap depth arising from the latter definition is discussed in the following, whereas the trap depths arising from both models are plotted in Fig. 2(d) for comparison.

To evaluate explicitly the trap depth within model 2, the maximum radius, r_{max}, such that $\eta(\hat{r}_{\text{max}},\hat{z}) \leqslant \eta_{\text{max}}$ is fulfilled for all $\hat{z}$ must be found. At a constant radius, the maximum value of η along $\hat{z}$ occurs at $\hat{z} = (2k+1)\pi/2$, where k is an integer, and hence the maximum radius is obtained by solving the equation $\eta(\hat{r}_{\text{max}},\pi/2) = \eta_{\text{max}}$, which reduces to

$$\eta_{\text{max}} = \frac{2qeV_0}{m\omega^2 z_0^2 I_0(\hat{r}_0)}\,|I_1(\hat{r}_{\text{max}})|\,. \tag{11}$$

$\hat{r}_{\text{max}}$ cannot be expressed analytically and must be determined numerically. At low RF amplitudes, $\hat{r}_{\text{max}}$ is larger than the geometrical trap radius, $\hat{r}_0$, implying that the radius of the trapping volume, $\hat{r}_{\text{trap}}$, has to be taken as the minimum of

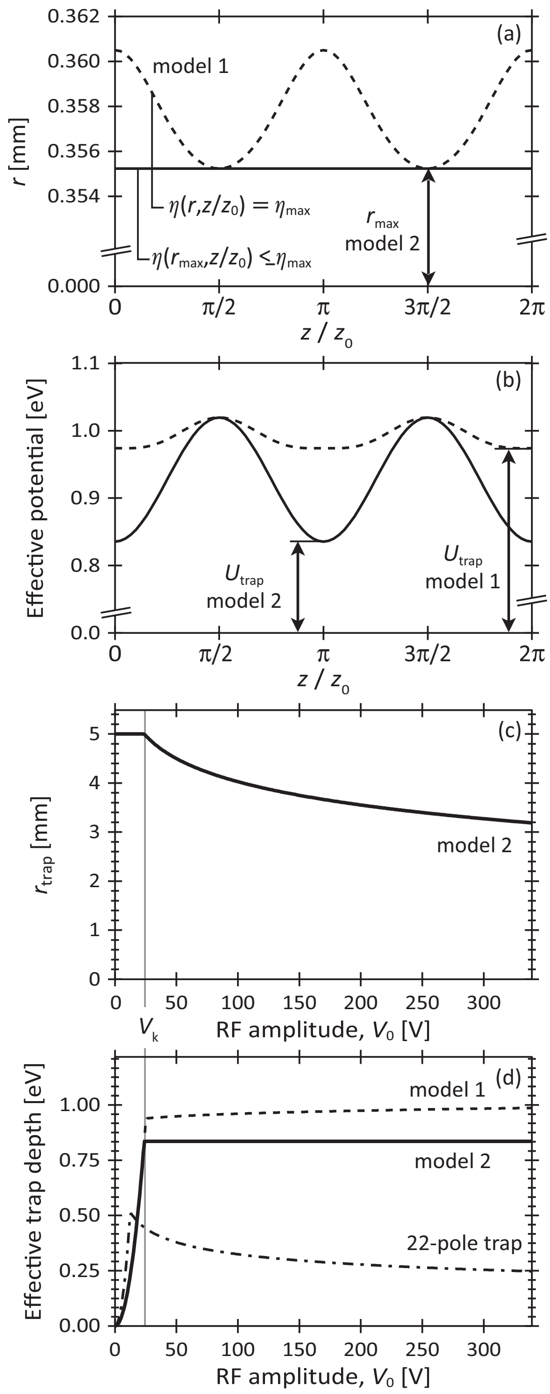

FIG. 2. Trapping volume and trap depth for the ring electrode trap according to two different models. (a) Boundary of the trapping volume for the two models at an RF amplitude of 200 V. The dashed line represents the boundary of the trapping volume of model 1 and the solid line that of model 2. (b) The effective potential along the boundary of the trapping volume for model 1 (dashed line) and model 2 (solid line) at an RF amplitude of 200 V. Drawn also is the trap depth for the two models. (c) The radius of the cylindrical trapping volume, $z_0\hat{r}_{\rm trap}$, for model 2. (d) The solid line represents the trap depth given by Eqs. (13) and (15) as a function of the RF amplitude, whereas the dashed line shows the trap depth arising from model 1, not discussed in detail. The dash-dotted line represents the trap depth of a 22-pole trap with an inscribed radius, r_0, of 5 mm [25]. The parameters used in all cases were $m = 56$ amu, $\omega = 2\pi \times 4$ MHz, and $\eta_{\max} = 0.30$.

the two radii:

$$\hat{r}_{\rm trap} = \min(\hat{r}_{\max},\hat{r}_0), \tag{12}$$

Thus, for RF amplitudes below a certain characteristic value, $V_{\rm k}$, the radius of the trapping volume is simply $\hat{r}_{\rm trap} = \hat{r}_0$, and in this regime the trap depth is the minimum of the effective potential at the electrode surface along $\hat{z}$. Since $U_{\rm eff}$ for a constant radial position exhibits minima at $\hat{z} = k\pi$, where k is an integer [see Fig. 2(b)], the trap depth is then given by

$$U_{\rm trap} = U_{\rm eff}(\hat{r}_0,\pi) = \frac{q^2e^2I_1^2(\hat{r}_0)}{4m\omega^2z_0^2I_0^2(\hat{r}_0)}V_0^2, \quad V_0 \leqslant V_{\rm k}. \tag{13}$$

At RF amplitudes above the characteristic value, $V_{\rm k}$, the ion motion is unstable in the outer regions of the trap, implying that $\hat{r}_{\rm trap} < \hat{r}_0$, and the trap depth is no longer given by the expression above [Eq. (13)]. The RF amplitude at which this regime is entered is found by solving the equation $\eta_{\max} = \eta(\hat{r}_0,\pi/2)$, yielding

$$V_{\rm k} = \frac{\eta_{\max}m\omega^2z_0^2I_0(\hat{r}_0)}{2qe\,|I_1(\hat{r}_0)|}. \tag{14}$$

Above this amplitude, the trap depth is the minimum of the effective potential along $\hat{z}$ for $\hat{r} = \hat{r}_{\max}$ which gives

$$\begin{aligned} U_{\rm trap} &= U_{\rm eff}(\hat{r}_{\max},\pi) = \frac{q^2e^2I_1^2(\hat{r}_{\max})}{4m\omega^2z_0^2I_0^2(\hat{r}_0)}V_0^2 \\ &= \frac{\eta_{\max}^2m\omega^2z_0^2}{16} = U_{\rm trap,max}, \quad V_0 \geqslant V_{\rm k}, \end{aligned} \tag{15}$$

where Eq. (11) has been used to eliminate $I_1(\hat{r}_{\max})$ and the maximum trap depth, $U_{\rm trap,max}$, has been introduced. According to the above equations, Eqs. (13) and (15), the trap depth increases quadratically with the RF amplitude until $V_{\rm k}$, after which point it remains constant at the value $U_{\rm trap,max}$. The trapping radius, $z_0\hat{r}_{\rm trap}$, and the trap depth are plotted in Figs. 2(c) and 2(d), respectively, with parameters relevant to the experiments with $\mathrm{Si_2}^-$ presented here. In this example, the trap depth becomes constant at an amplitude of $V_{\rm k} = 24$ V at which point $\hat{r}_{\max}$ becomes equal to the geometrical radius. For comparison, the trap depth emerging from model 1 is also shown. The two models give similar results, though the trap depth is somewhat larger and increasing slightly for $V_0 \geqslant V_{\rm k}$ in the case of model 1. The functional dependence of the trap depth on the RF amplitude is characteristic of the trap geometry, and in the case of the ring electrode trap, the trap depth remains constant at RF amplitudes above $V_{\rm k}$. In contrast, the trap depth for a 22-pole trap [25] is decreasing above the characteristic RF amplitude at which the radius of the trapping volume equals the geometrical radius [see Fig. 2(d)].

The equations presented above are applicable during storage of ions in the trap and reveal that the translational energy of ions injected into the trap must be lower than ~1 eV, the radial trap depth, in order to be stored.

III. ANALYTICAL DESCRIPTION OF ION INJECTION FROM A FAST ION BEAM

A. Ion injection from a fast ion beam

In this section, it is described how fast ions of keV energies can be loaded into a ring electrode trap. As only ions with energies of a few eVs are confined, the overall potential of the trap, V_{trap}, is offset from ground potential in order to decelerate ions before entering the trap. The shallow trap depth would imply that the matching between the initial ion energy and the ion potential energy at the trap center (qeV_{trap}) is critical. This turns out, however, not to be the case for the ring electrode trap. The special geometry of the ring electrode trap gives rise to a *longitudinal* RF field in the region between the entrance end cap and the first ring electrode, and this longitudinal field modulates the ion energy when entering the trap (see Fig. 3). Consequently, the ion potential energy in the trap need not be carefully matched to the initial ion beam energy.

The situation encountered here is similar to passing ions through a linear RF accelerator (linac) [29] in which ions are accelerated or decelerated depending on the RF phase upon their arrival. Hence, the approach taken to describe the operation of a linac [29] may be suited to estimate the effect of the longitudinal RF field on the ion kinetic energy in the case of the ring electrode trap. In the following, this route is pursued to derive analytical expressions for conditions for ion trapping and their dependence on the RF amplitude and phase.

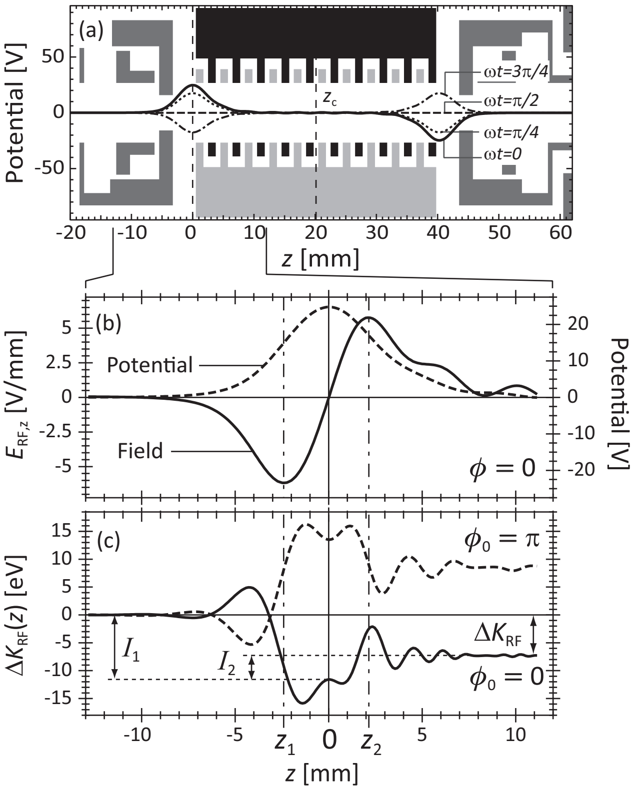

FIG. 3. The longitudinal RF field and its influence on the ion kinetic energy. (a) The electric potential along the trap axis when a potential of $+100$ V × $\cos\omega t$ is applied to the ring electrode set containing the first electrode (light gray electrodes) while -100 V × $\cos\omega t$ is applied to the other ring electrode set (black electrodes). All other electrodes are kept at ground potential. The potential is shown at different times such that $\omega t = k \times \pi/4$, where k is 0 (solid line), 1 (dotted line), 2 (dashed line), or 3 (dash-dotted line). The zero point of the z axis is chosen at the position of the peak potential on the entrance side. The trap center, z_c, is at approximately 20 mm. (b) The electric potential (dashed curve) and the corresponding longitudinal electric field (solid curve) on the trap axis due to the RF field at the RF phase $\phi = 0$. Also shown are the points, z_1 and z_2, at which the electric field peaks. (c) The influence of the longitudinal field on the ion kinetic energy when the ion crosses $z = 0$ at two different RF phases. The simulation (see details in Sec. IV) is done for a $\mathrm{Si_2}^-$ ion with a nominal kinetic energy of $K_{\mathrm{stat}} = 10$ eV and at an RF amplitude of $V_0 = 200$ V.

In classical mechanics, the energy exchange between the ion and the electric field is described through the work-energy theorem stating that the change in kinetic energy, ΔK, of an ion arriving at the trap center, z_c, is equal to the net work done by the field, i.e.,

$$\Delta K = qe\int_{-\infty}^{z_c} \vec{E}(\vec{r},t)\cdot d\vec{r} = qe\int_{-\infty}^{z_c} [\vec{E}_{\mathrm{stat}}(\vec{r}) + \vec{E}_{\mathrm{RF}}(\vec{r},t)]\cdot d\vec{r} \\ = \Delta K_{\mathrm{stat}} + \Delta K_{\mathrm{RF}}. \tag{16}$$

Here, $\vec{E}_{\mathrm{stat}}(\vec{r})$ is the static component of the electric field, in the present case stemming from the static potentials applied to the various electrodes in the trap assembly, and $\vec{E}_{\mathrm{RF}}(\vec{r},t)$ is the time-dependent component of the electric field arising from the RF potentials applied to the ring electrodes. ΔK_{stat} and ΔK_{RF} are the changes in kinetic energy due to the static and time-dependent fields, respectively. For an ion to be trapped, it is necessary that it reaches the trap center and that its kinetic energy at this point is lower than the trap depth resulting in the following criterion:

$$0 \leqslant K_0 + \Delta K \leqslant U_{\mathrm{trap}}. \tag{17}$$

Here, K_0 is the ion kinetic energy far from the trap center and U_{trap} the trap depth from Eqs. (13) and (15). Equation (17) thus states the general criterion for whether or not an injected ion becomes trapped, and this expression is now analyzed in more detail.

First, the contribution to the kinetic energy change from the static field alone is examined. For simplicity, only the longitudinal energy loss of an ion on the trap axis (the z axis) is considered. In absence of the RF field, the change in kinetic energy for an ion arriving at the trap center, z_c, is

$$\Delta K_{\mathrm{stat}} = qe\int_{-\infty}^{z_c} \vec{E}_{\mathrm{stat}}(z)\cdot d\vec{z} = -qe\Delta V = -qeV_{\mathrm{trap}}, \tag{18}$$

yielding a kinetic energy at z_c of

$$K_{\mathrm{stat}} = K_0 + \Delta K_{\mathrm{stat}} = K_0 - qeV_{\mathrm{trap}}, \tag{19}$$

where again K_0 is the ion beam energy far from the trap, and V_{trap} the overall electric potential of the trap which is offset from ground potential. Hence, K_{stat} is the resulting kinetic energy for a conservative force and is referred to as the *nominal* kinetic energy.

Second, when the RF field is also present, the ions are in addition subjected to a nonconservative force, and consequently their kinetic energy at the trap center now deviates from K_{stat}. Snapshots of the RF potential along the trap axis are shown in Fig. 3(a), and the zero point of the z axis is chosen at the position where this potential peaks. As an ion traverses the region around $z = 0$, the potential is oscillating, and the kinetic energy change thus depends on the detailed oscillation of the potential during the traversal. This fact is illustrated in Fig. 3(c), which shows the change in kinetic energy due to the RF field for two ions that cross $z = 0$ at different RF phases. The details of the energy oscillations are hard to describe analytically, but an approximate expression for the total kinetic energy change due to the RF field, ΔK_{RF}, can be derived following the approach of Weiss [29] and Wadlinger and co-workers [30]. Thus, for an ion traveling on the z axis, the RF-induced kinetic energy change when arriving at the trap center is given by

$$\begin{aligned}\Delta K_{\mathrm{RF}} &= qe\int_{-\infty}^{z_c} E_{\mathrm{RF},z}(z,t)dz\\ &= qe\int_{-\infty}^{z_c} E_{\mathrm{RF},z}(z,0)\cos[\omega t(z)]dz,\end{aligned}\tag{20}$$

where $E_{\mathrm{RF},z}$ is the z component of the RF field. Generally, the equation of motion cannot be solved analytically, implying that an analytical expression for $t(z)$ cannot be given. To proceed, the ion velocity during the passage through the entrance RF field is approximated by a constant, v_{ion}. This approximation, which is also introduced in the case of linacs [29], seems crude, but the final result provides a good description of the simulated results, as demonstrated in Sec. IV A. Consequently, the ion velocity, v_{ion}, is considered a constant and taken to be the mean velocity during the passage. A value for v_{ion} may thus be determined by solving the ion equation of motion and then extracting the mean velocity through this region of interest. At $t = 0$, the ion crosses $z = 0$ at a particular phase, ϕ_0, of the RF field, implying that $\omega t(z) = \omega z/v_{\mathrm{ion}} + \phi_0$, and Eq. (20) can therefore be written as

$$\Delta K_{\mathrm{RF}} \approx qe\int_{-\infty}^{z_c} E_{\mathrm{RF},z}(z,0)\cos\left(\frac{\omega z}{v_{\mathrm{ion}}} + \phi_0\right)dz.\tag{21}$$

This expression may be elaborated upon by considering the properties of the electric field displayed in Fig. 3(b) along with the RF potential. As seen, the electric field exhibits two extrema analogous to the situation encountered in a double-gap acceleration cell [30]. This implies that the total kinetic energy change, ΔK_{RF}, contains two contributions: one contribution, I_1, from the kinetic energy change achieved during the traversal of the first peak in the electric field, and another contribution, I_2, from the traversal of the second peak [see Fig. 3(c)]. The integration in Eq. (21) is therefore split into these two parts, yielding

$$\begin{aligned}\Delta K_{\mathrm{RF}} &= qe\int_{-\infty}^{0} E_{\mathrm{RF},z}(z,0)\cos\left(\frac{\omega z}{v_{\mathrm{ion}}} + \phi_0\right)dz\\ &\quad + qe\int_{0}^{z_c} E_{\mathrm{RF},z}(z,0)\cos\left(\frac{\omega z}{v_{\mathrm{ion}}} + \phi_0\right)dz\\ &\equiv I_1 + I_2.\end{aligned}\tag{22}$$

The two integrals may be brought to a more accessible form by introducing the two points, z_1 and z_2, at which the electric field exhibits its extrema [see Fig. 3(b)]. By doing so, the first contribution to the energy change, I_1, may be written as

$$\begin{aligned}I_1 &= qe\int_{-\infty}^{0} E_{\mathrm{RF},z}(z,0)\cos\left(\frac{\omega(z-z_1)}{v_{\mathrm{ion}}} + \phi_0 + \frac{\omega z_1}{v_{\mathrm{ion}}}\right)dz\\ &= qe\int_{-\infty}^{0} E_{\mathrm{RF},z}(z,0)\cos\left(\frac{\omega(z-z_1)}{v_{\mathrm{ion}}} + \phi_1\right)dz\\ &= qe\int_{-\infty}^{0} E_{\mathrm{RF},z}(z,0)\cos\frac{\omega(z-z_1)}{v_{\mathrm{ion}}}\cos\phi_1 dz\\ &\quad - qe\int_{-\infty}^{0} E_{\mathrm{RF},z}(z,0)\sin\frac{\omega(z-z_1)}{v_{\mathrm{ion}}}\sin\phi_1 dz,\end{aligned}\tag{23}$$

where $\phi_1 = \phi_0 + \omega z_1/v_{\mathrm{ion}}$ is the phase of the RF field when the ion crosses $z = z_1$. From Fig. 3(b), it is seen that the electric field along the trap axis for $z < 0$ is approximately an even function with respect to $z - z_1$, wherefore the last integral in Eq. (23) vanishes, thereby yielding

$$I_1 \approx qe\cos\phi_1\int_{-\infty}^{0} E_{\mathrm{RF},z}(z,0)\cos\frac{\omega(z-z_1)}{v_{\mathrm{ion}}}dz.\tag{24}$$

To express explicitly the dependence of I_1 on the RF amplitude, V_0, and the phase, ϕ_1, the so-called *transit-time factor*, T_1', is introduced:

$$T_1' = \frac{1}{V_0}\int_{-\infty}^{0} E_{\mathrm{RF},z}(z,0)\cos\frac{\omega(z-z_1)}{v_{\mathrm{ion}}}dz.\tag{25}$$

T_1' describes the influence on the energy change due to the finite time it takes the ion to traverse the region around the first peak of the RF field. Since $V_{\mathrm{RF}}(\vec{r},t) \propto V_0$ and $\vec{E}_{\mathrm{RF}}(\vec{r},t) = -\vec{\nabla}V_{\mathrm{RF}}(\vec{r},t)$ [31], it follows directly that $\vec{E}_{\mathrm{RF}}(\vec{r},t) \propto V_0$, and T_1' therefore depends on V_0 only indirectly through the influence of the RF field on the ion velocity [33]. If the velocity change due to the RF field is small compared to v_{ion}, the dependence of T_1' on V_0 can then largely be neglected (the simulations presented in Sec. IV A and Fig. 6 reveal that the velocity change is of the order of 10% of the mean ion velocity in this spatial region, indicating the validity of this approximation). The final expression for I_1 is then written as

$$I_1 \approx qeV_0T_1'\cos\phi_1.\tag{26}$$

Similarly, by introducing the point, z_2 [see Fig. 3(b)], the RF phase, $\phi_2 = \phi_0 + \omega z_2/v_{\mathrm{ion}}$, at which the ion crosses this point, and by exploiting that the RF electric field for $z > 0$ is approximately symmetric around $z = z_2$, the second contribution to the kinetic energy change, I_2, is expressed as

$$I_2 \approx qeV_0T_2'\cos\phi_2,\tag{27}$$

where T_2' is the transit-time factor for traversing the second peak of the electric field:

$$T_2' = \frac{1}{V_0}\int_{0}^{z_c} E_{\mathrm{RF},z}(z,0)\cos\frac{\omega(z-z_2)}{v_{\mathrm{ion}}}dz.\tag{28}$$

The total change in kinetic energy due to the RF field now reads

$$\Delta K_{\mathrm{RF}} = qeV_0[T_1'\cos\phi_1 + T_2'\cos\phi_2].\tag{29}$$

The mean velocity through the longitudinal field is to a great extent controlled by the potential applied to the entrance end cap and, provided this potential is chosen such that the ion velocity, v_{ion}, fulfills the relations $\omega|z_1|/v_{\mathrm{ion}} \simeq \omega|z_2|/v_{\mathrm{ion}} \simeq \pi$, Eq. (29) is further reduced to

$$\begin{aligned}\Delta K_{\mathrm{RF}} &= qeV_0[T_1'\cos(\phi_0 - \pi) + T_2'\cos(\phi_0 + \pi)]\\ &= -qeV_0\cos\phi_0[T_1' + T_2'] = -qeV_0T_{\mathrm{eff}}'\cos\phi_0,\end{aligned}\tag{30}$$

where $T_{\mathrm{eff}}' = T_1' + T_2'$ is the *effective* transit-time factor for traversing both peaks of the electric field.

The behavior of the simulated kinetic energy change illustrated in Fig. 3(c) can now be examined in light of the derivation above. In the simulations (see Sec. IV for further details), $\omega = 2\pi \times 4$ MHz and the mean ion velocity, v_{ion}, is 17 mm/μs, with the result that $\omega|z_1|/v_{\mathrm{ion}} \simeq \omega|z_2|/v_{\mathrm{ion}} \simeq \pi$, implying that Eq. (30) should provide a fair description of the energy change. From Fig. 3(b), it is seen that $E_{\mathrm{RF},z}(z,0) < 0$ for $z < 0$, resulting in $T_1' < 0$ from Eq. (25). As the simulations presented in Fig. 3(c) were done for a negative ion, $q = -1$ and as $\cos\phi_0 = 1$ for $\phi_0 = 0$, Eq. (26) predicts that $I_1 < 0$ for the ion that crosses $z = 0$ at $\phi_0 = 0$. This corresponds to an initial deceleration of the ion in agreement with the simulations shown in Fig. 3(c). The second contribution to the energy change, I_2, is of the opposite sign since $E_{\mathrm{RF},z}(z,0) > 0$ for $z > 0$, implying that $T_2' > 0$ for $\phi_0 = 0$ in which case this same ion is accelerated during the traversal of the last part of the region, also in agreement with the simulations. Figure 3(b) shows that the absolute value of the electric field is higher at z_1 than z_2, resulting in $|T_1'| > |T_2'|$. Consequently, the initial deceleration is larger than the following acceleration, and the net effect is therefore a *deceleration* of the ion (corresponding to $T_{\mathrm{eff}}' < 0$) in accordance with the observations. If, instead, the ion crosses $z = 0$ at the phase $\phi_0 = \pi$, the sign of both terms, I_1 and I_2, is changed as $\cos\phi_0 = -1$ and the ion is now initially accelerated and then decelerated to a lesser extent, yielding an overall *acceleration* for $\phi_0 = \pi$.

With Eq. (30), the general criteria, Eq. (17), for trapping ions that have traversed the longitudinal RF field can be analyzed. Using Eqs. (16), (19), and (30) in Eq. (17), the criteria for trapping now reads

$$\begin{aligned} 0 \;&\leqslant\; K_{\mathrm{stat}} + \Delta K_{\mathrm{RF}} \leqslant U_{\mathrm{trap}} \\ \iff -K_{\mathrm{stat}} \;&\leqslant\; -qeV_0T_{\mathrm{eff}}'\cos\phi_0 \;\leqslant\; U_{\mathrm{trap}} - K_{\mathrm{stat}}. \end{aligned} \tag{31}$$

If the nominal kinetic energy is larger than the trap depth, that is $K_{\mathrm{stat}} > U_{\mathrm{trap}}$, it follows from this equation that $\Delta K_{\mathrm{RF}} \leqslant 0$, and trapping only occurs provided the RF field *dissipates* the excess kinetic energy. In this case, the ion must cross $z = 0$ at $\phi_0 = 0$ to be trapped according to the analysis above. If instead $K_{\mathrm{stat}} < 0$, that is, the ion potential energy at the trap center is larger than the initial ion energy, $\Delta K_{\mathrm{RF}} \geqslant 0$, in which case the RF field must *accelerate* the ions to obtain trapping. Correspondingly, ions must now arrive at $z = 0$ at the phase $\phi_0 = \pi$.

The consequences of the above inequalities are illustrated in Fig. 4(a) in the case of a fixed nominal kinetic energy at which $K_{\mathrm{stat}} > U_{\mathrm{trap}}$. As seen, an incoming ion is accelerated or decelerated by the RF field of amplitude V_0 depending on the RF phase when the ion crosses $z = 0$. Consequently, the above inequalities for fixed K_{stat} and V_0 are fulfilled only for certain phase intervals depicted by the gray areas in Fig. 4(a), and trapping is hence only achieved for ions arriving at these phases. To describe how these trapping phase intervals change with RF amplitude, an expression for the mean phase, $\phi_{0,\mathrm{m}}$, shown in Fig. 4(a) is sought. At this phase, the energy change equals the mean required energy change to obtain trapping, $\Delta K_{\mathrm{RF,mean}}$. Equation (31) states the upper and lower limits of the energy change, and from these extremes, $\Delta K_{\mathrm{RF,mean}}$ is found to be

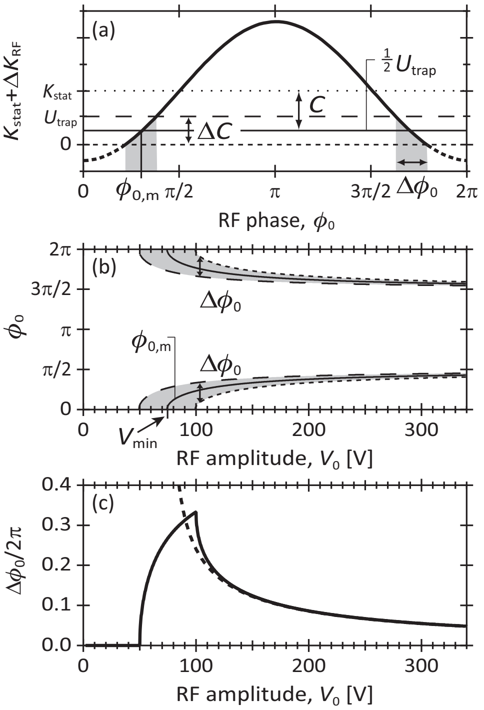

FIG. 4. Illustrations of the criteria for trapping mediated by the longitudinal RF field. (a) The thick black curve represents at a fixed RF amplitude the ion kinetic energy at z_c as a function of the RF phase experienced at $z = 0$. The curve is dashed in the phase interval, yielding negative kinetic energies corresponding to phases where the ion after traversal of the longitudinal field does not carry enough energy to reach the trap center. The short-dashed and long-dashed lines represent the lower and upper bounds of the first inequalities of Eq. (31), respectively. The gray areas highlight the phase interval over which these inequalities are fulfilled and over which trapping is hence achieved. (b) The relationship between the RF amplitude and phase that results in the energy change necessary for trapping. The black line shows the relationship predicted by Eq. (33) while the gray area shows the phase interval within which Eq. (31) is fulfilled. The short-dashed and long-dashed lines represent the lower and upper bounds of the first inequalities of Eq. (31), respectively, that is setting C in Eq. (33) to $-K$stat and $U_{\mathrm{trap}} - K$stat. (c) The solid line shows the fractional phase width of the gray phase area in (b), whereas the dashed line represents the fractional phase width over which ions can be trapped as a function of RF amplitude as described by Eq. (35).

$$\begin{aligned} \Delta K_{\mathrm{RF,mean}} &= \tfrac{1}{2}[-K_{\mathrm{stat}} + (U_{\mathrm{trap}} - K_{\mathrm{stat}})] \\ &= \tfrac{1}{2}U_{\mathrm{trap}} - K_{\mathrm{stat}} \equiv C. \end{aligned} \tag{32}$$

As U_{trap} only depends on the RF amplitude for small amplitudes [see Fig. 2(d)], $\Delta K_{\mathrm{RF,mean}}$ is roughly independent of V_0 and is for now considered to be a constant, C, for fixed K_{stat}. Setting $\Delta K_{\mathrm{RF}} = C$ in Eq. (30) and rearranging yields the following relationship between the RF amplitude and the RF phase leading to the mean required energy change:

$$-\frac{C}{qeT_{\mathrm{eff}}'} = V_0\cos\phi_{0,\mathrm{m}}. \tag{33}$$

The left side of this equation is merely a constant since T_1' and T_2', and thereby T_{eff}', are roughly independent of V_0 as already mentioned. As $|\cos\phi_{0,\mathrm{m}}| \leqslant 1$, this equation is fulfilled only if

$$V_0 \geqslant |V_{\min}| = \left| -\frac{C}{qeT'_{\mathrm{eff}}} \right|. \tag{34}$$

This implies that for a given nominal kinetic energy, K_{stat}, a minimum RF amplitude, $|V_{\min}|$, is needed to change the kinetic energy by the required amount. At this minimum amplitude, ions are trapped at either $\cos\phi_{0,\mathrm{m}} = 1$ or $\cos\phi_{0,\mathrm{m}} = -1$, depending on the sign of C, which indicates whether ions must be decelerated or accelerated to achieve trapping. These features are illustrated in Fig. 4(b), which depicts the relationship between the RF amplitude and phase predicted by Eq. (33). As argued above, ions can be trapped provided their kinetic energy at the trap center is between 0 eV and the trap depth. Correspondingly, trapping is still achieved for amplitudes, V_0, and phases, ϕ, fulfilling Eq. (33) with $\phi_{0,\mathrm{m}} = \phi$ and C in the range between $-K_{\mathrm{stat}}$ [short-dashed line in Fig. 4(b)] and $U_{\mathrm{trap}} - K_{\mathrm{stat}}$ [long-dashed line in Fig. 4(b)], resulting in trapping within the gray area of Fig. 4(b).

Figures 4(a) and 4(b) illustrate that the finite width of the required kinetic energy change, ΔC, leads to trapping in some phase interval. The width of this phase interval, $\Delta\phi_0$, is indicative of the trapping probability for ions traversing the field at random phases at $z = 0$. The relative phase width, $\Delta\phi_0/2\pi$, of the gray area in Fig. 4(b) is plotted in Fig. 4(c) as a function of the RF amplitude (solid line). As seen, the phase width is initially zero, implying that at low RF amplitudes the RF field is not strong enough to induce the required energy change. At the RF amplitude where the upper limit in Eq. (31) is reached, the phase width begins to increase until the RF amplitude at which the lower limit in Eq. (31) is reached. After this point, the phase width is constantly decreasing, implying that trapping occurs only for two narrow phase windows at large RF amplitudes.

A simple expression for the asymptotic behavior of the phase width is obtained by differentiation of Eq. (33):

$$\Delta\phi_0 \simeq 2\Delta C \left| \frac{\partial\phi_{0,\mathrm{m}}}{\partial C} \right| = 2\Delta C \left| \frac{\partial}{\partial C} \arccos \frac{-C}{qeT'_{\mathrm{eff}}V_0} \right| = \frac{2\Delta C}{|qeT'_{\mathrm{eff}}|\sqrt{V_0^2 - V_{\min}^2}}, \tag{35}$$

where the factor of 2 is introduced since the arccos function used here describes only one branch of the otherwise multivalued function. The expression is plotted as the dashed line in Fig. 4(c) and yields a good description of the asymptotic behavior of the phase width.

B. Trapping efficiency

The trapping efficiency, ε, here defined as the fraction of incoming ions that become trapped, can be estimated within the analytical model developed in the previous section. In doing so, two assumptions are made: (1) the incoming ions cross $z = 0$ at phases uniformly distributed over the entire phase of the RF field and (2) ions are trapped with 100% probability provided their kinetic energy when first arriving at the trap center is between 0 eV and the trap depth. In this case, the trapping efficiency is simply equal to the fractional phase width ($\Delta\phi_0/2\pi$) defined above:

$$\varepsilon = \Delta\phi_0/2\pi. \tag{36}$$

Its functional dependence on both the RF amplitude, V_0, and the nominal kinetic energy, K_{stat}, is determined by calculating the fractional phase width over which Eq. (31) is fulfilled. At some fixed nominal kinetic energy where $K_{\mathrm{stat}} > U_{\mathrm{trap}}$, the RF amplitude dependence of the fractional phase width, and hence the trapping efficiency, was already shown by the solid line in Fig. 4(c). Thus, it is likely concluded that the trapping efficiency as a function of the RF amplitude for fixed K_{stat} always exhibits a behavior similar to that in Fig. 4(c). However, in the derivation of Eq. (33), which was used to determine the fractional phase width, U_{trap} was assumed to be a constant independent of the RF amplitude. This assumption is valid provided that trapping occurs only at RF amplitudes in the range where the trap depth is constant, that is, $V_{\min} > V_{\mathrm{k}}$ [see Fig. 2 and Eq. (34)]. If trapping occurs at RF amplitudes lower than V_{k}, this assumption is no longer valid, in which case the gray area of Fig. 4(b) has a more complicated shape (see Fig. 7 and comments relating to this figure). As a result, the fractional phase width, and hence the trapping efficiency, for fixed K_{stat} does not merely behave as the solid line in Fig. 4(c) if trapping is achieved at low RF amplitudes. Therefore, the dependence of U_{trap} on V_0 described by Eqs. (13) and (15) must generally be taken into account when determining the fractional phase width over which Eq. (31) is fulfilled.

When calculating the trapping efficiency, also T'_{eff} must be considered. To a first approximation, T'_{eff} is independent of V_0 as already argued. It does, however, depend on K_{stat}. This is true since K_{stat} depends on the trap potential, V_{trap} [Eq. (18)], which in turn influences the mean ion velocity, v_{ion}, entering into T'_{eff}. The mean ion velocity is furthermore affected by the potentials applied to the entrance end cap and lens. It turns out that for the potentials applied in the present experiments these electrodes to a very large extent solely control the mean ion velocity over the relevant K_{stat} range. Consequently, T'_{eff} is considered to be a constant when determining the trapping efficiency.

Figure 5 shows the resulting trapping efficiency as a function of both the RF amplitude and the nominal kinetic energy where the only free parameters, T'_{eff} and $\eta_{\max}$, are chosen to obtain the best agreement with the simulations presented in Sec. IV A ($T'_{\mathrm{eff}} = -0.035$ and $\eta_{\max} = 0.64$; see Sec. IV A1 for comments regarding the value of $\eta_{\max}$). As indicated by the solid white lines, the RF amplitude at which maximum trapping efficiency is achieved for a given K_{stat} changes linearly with K_{stat} except in the region of low kinetic energy and low RF amplitudes where the lines are now dashed. This is a manifestation of Eq. (34) in which C depends linearly on K_{stat}, as seen from Eq. (32), and the slope is inversely proportional with T'_{eff} as seen from Eq. (34). Consequently, the opening angle, θ, of the "<"-shaped contour lines indicated on the figure is controlled by T'_{eff}, which depends on the ion energy upon entering the longitudinal RF field. As already argued, this energy is dependent on the potentials applied to the entrance end cap and lens, and hence changing these potentials affects this opening angle. Furthermore, the outermost contour lines exhibit linear behavior with RF amplitude for $K_{\mathrm{stat}} < 0$ but display a kink around $V_0 = 50$ V for $K_{\mathrm{stat}} > 0$, which is a result

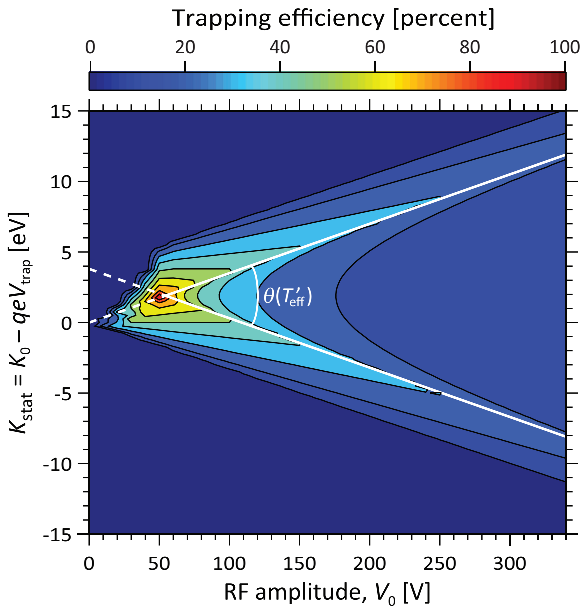

FIG. 5. (Color online) The trapping efficiency, ε [Eq. (36)], obtained within the analytical model as a function of the nominal kinetic energy and the RF amplitude. In the calculations, T'_{eff} was assumed to be a constant independent of V_0 and K_{stat} and was set to -0.035 and $\eta_{\max}$ to 0.64 to obtain good agreement with simulations presented in Sec. IV A (see Fig. 8). Solid white lines display the relationship between V_0 and K_{stat}, leading to maximum trapping efficiency.

of the increasing trap depth for low RF amplitudes. Finally, it is noted that maximum trapping efficiency is achieved for $K_{\mathrm{stat}} > 0$, which is a natural consequence of the boundaries put on the kinetic energy from Eq. (31). When traversing the longitudinal field, half of the incoming ions are decelerated while the other half are accelerated according to Fig. 4. Maximum trapping efficiency therefore occurs when both these classes of ions can still be trapped, in which case $K_{\mathrm{stat}} \simeq \frac{1}{2}U_{\mathrm{trap}}$.

IV. NUMERICAL SIMULATIONS

To validate and explore the approximate analytical model developed in Sec. III, Monte Carlo simulations were performed using the SIMION software [34]. The Laplace equation for the electric potential of the electrode configuration of the ring electrode trap was solved on a grid with a spatial resolution of 0.25 mm. Ion motion in the obtained potential was subsequently investigated by propagating ions from a randomized sample. Thus, 5000 ions of mass 56 amu and charge $qe = -1e$, simulating $\mathrm{Si}_2{}^-$ ions, were initialized on ground potential at a fixed axial distance from the trap. Spatially, the ions were distributed evenly around the trap axis according to a Gaussian radial distribution with a FWHM radius of 2 mm, and they were started with equal velocities having only a nonzero component in the axial direction towards the trap. The initial ion kinetic energy, K_0, was set to 3 keV, and, in the absence of nonconservative forces (that is, only static electric fields are present), the nominal kinetic energy of the ions arriving at the trap center, K_{stat}, is given as $K_{\mathrm{stat}} = K_0 - qeV_{\mathrm{trap}}$ [Eq. (19)], where V_{trap} is the trap platform potential. The start time of the ions (the ion time of birth) was distributed uniformly in the time window between 0 and 30 μs, during which time the potential of the entrance electrode was kept positive with respect to the platform potential to let the negative ions enter the trap. After 30 μs, the entrance potential was switched instantaneously to a negative value in order to trap ions for 500 μs, whereafter the potential of the exit end cap was switched to extract ions from the trap. Ions were considered to be stably trapped if they remained trapped during the whole 500-μs-long trapping period, and the trapping efficiency was then obtained as the ratio of stably trapped ions to the total number of injected ions. Similar simulations were performed for different amplitudes of the radially confining RF potential and for different nominal kinetic energies, K_{stat}, by varying the trap platform potential, V_{trap}, while the potentials of the remaining electrodes were set to the values used in the experiments presented later.

A. Simulated trapping dynamics and comparison to the analytical model

1. The loading principle

Figure 6 shows the distribution of ion kinetic energies at $z = 0$ [see Fig. 3(a)] as a function of RF amplitude, V_0, for a fixed nominal kinetic energy of $K_{\mathrm{stat}} = 6$ eV. Note that the kinetic energy at this point is much larger than the nominal kinetic energy as it is influenced by the potentials applied to the entrance end cap and lens (see Fig. 1). The results clearly demonstrate that the RF field perturbs the energy distribution and that it effectively accelerates or decelerates the ions.

The white line in Fig. 6 outlines the energy region within which the kinetic energy of ions that become trapped appears. For the presented results, the nominal kinetic energy of 6 eV is somewhat higher than the trap depth [see Fig. 2(d)], and, consequently, ions must be decelerated to achieve trapping.

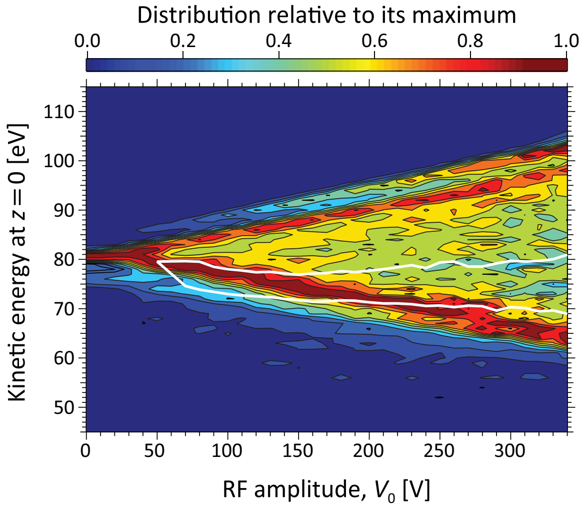

FIG. 6. (Color online) Effect of the RF field on the kinetic energy of the injected ions: Simulated distribution of ion kinetic energies at $z = 0$ plotted as a function of the RF amplitude when the nominal kinetic energy was set to 6 eV. The region bounded by the white line is the energy region of ions that become trapped.

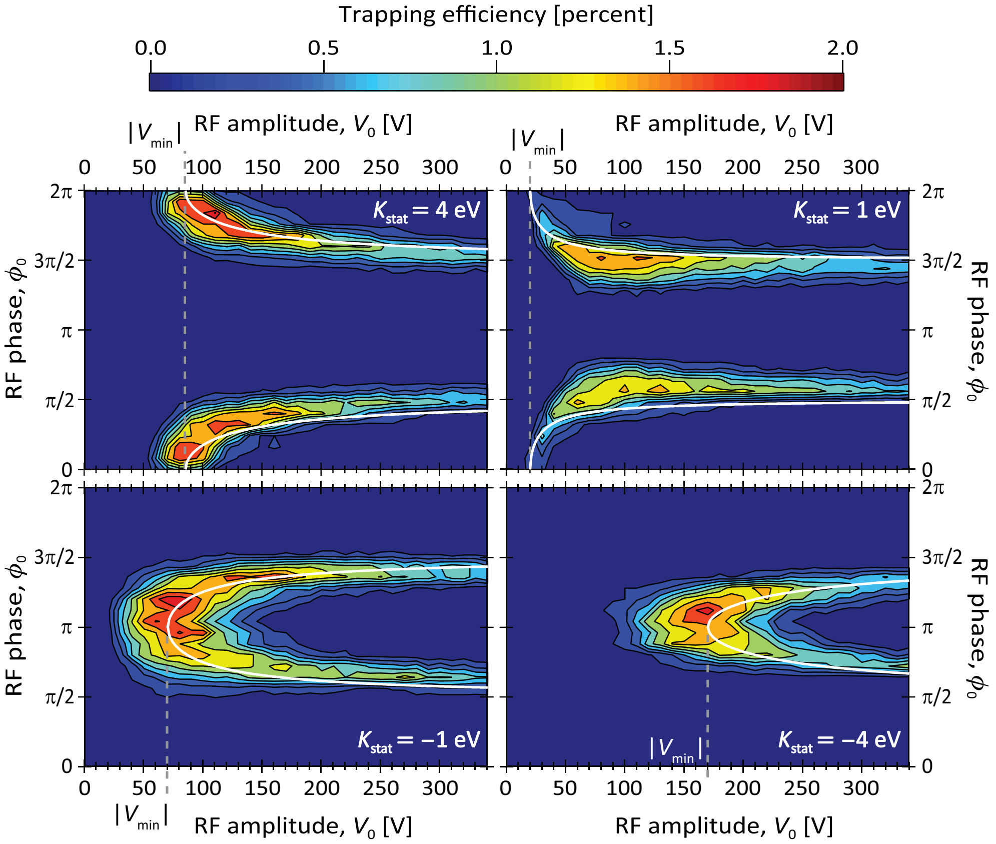

FIG. 7. (Color online) Relationship between RF phase and RF amplitude required for stable trapping of ions: Simulated trapping efficiency as a function of the RF amplitude and of the RF phase at $z = 0$, ϕ_0. The four plots are for different nominal kinetic energies as indicated on the individual graphs. The white curves represent the relationship between the phase and the RF amplitude for which the mean required energy change is achieved, according to Eq. (33).

This agrees well with the observation that the region leading to trapping is centered around an energy lower than the average ion energy of ~58 eV at zero RF field. Ions are not trapped at low RF amplitudes in this case since the RF field cannot dissipate enough energy at low amplitudes.

More details on the relationship between the RF phase and the RF amplitude needed to obtain trapping are shown in Fig. 7, which illustrates the trapping efficiency in dependencies of ϕ_0, V_0, and K_{stat}. When $K_{\text{stat}} \gtrsim U_{\text{trap}}$, ions must be decelerated to obtain trapping in which case trapped ions pass $z = 0$ around $\phi_0 = 0$, whereas they instead pass this point around $\phi_0 = \pi$ if they need to be accelerated ($K_{\text{stat}} < 0$). The simulated relationship between the RF phase and amplitude for the trapped ions is very well reproduced by Eq. (33) shown as the white lines in Fig. 7. This clearly verifies that energy exchange between the ions and the longitudinal RF field is the key to understanding the trapping dynamics for ions injected into the ring electrode trap at energies of the order of several tens of eV.

In Fig. 7, it should be noted that the RF amplitude-RF phase contours for $K_{\text{stat}} = 1$ eV have a slightly different shape than those plotted for the three other values of K_{stat}: First, the trapping efficiency is close to zero in the region around $\phi_0 = 0$ for low RF amplitudes, unlike the case for $K_{\text{stat}} = 4$ eV. Second, at RF amplitudes around 100 V the contour lines around $\phi_0 = \pi/2$ extend further towards π than for $K_{\text{stat}} = 4$ eV. Overall, the shape is somewhat different from the shape depicted in Fig. 4(b). This is a manifestation of the trap depth changing with RF amplitude which gives rise to more complicated shapes than the one illustrated in Fig. 4(b), which was derived assuming a constant trap depth.

The simulated trapping efficiency as a function of the nominal kinetic energy and the RF amplitude is shown in Fig. 8(a) in comparison to the analytical trapping efficiency shown in Fig. 5. As mentioned in Sec. III B, the two free parameters entering into the analytical trapping efficiency, namely $\eta_{\max}$ and T'_{eff}, have been chosen to best match the simulations yielding values of 0.64 and −0.035, respectively. Notably, the value of $\eta_{\max}$ is significantly higher than the 0.3 or 0.36 mentioned earlier. However, the value of 0.3 has been empirically determined as a criterion for safe operating conditions, but possibly several islands of stability may be localized at higher values of η [19]. In the injection scheme presented here, the RF field modulates the kinetic energy [see Fig. 4(a) and Fig. 9] of the incoming ions, which may lead to a population of stable or pseudostable trajectories with η in higher-lying stability regions. This circumstance is then reflected by the high $\eta_{\max}$ value. Most interesting, simulations by Gerlich [19] show a stable region at $\eta = 0.65$ in good correspondence with the $\eta_{\max}$ determined here.

The resemblance of the simulation and analytical model is quantified by the cross-sectional plots of Figs. 8(b) and 8(c),

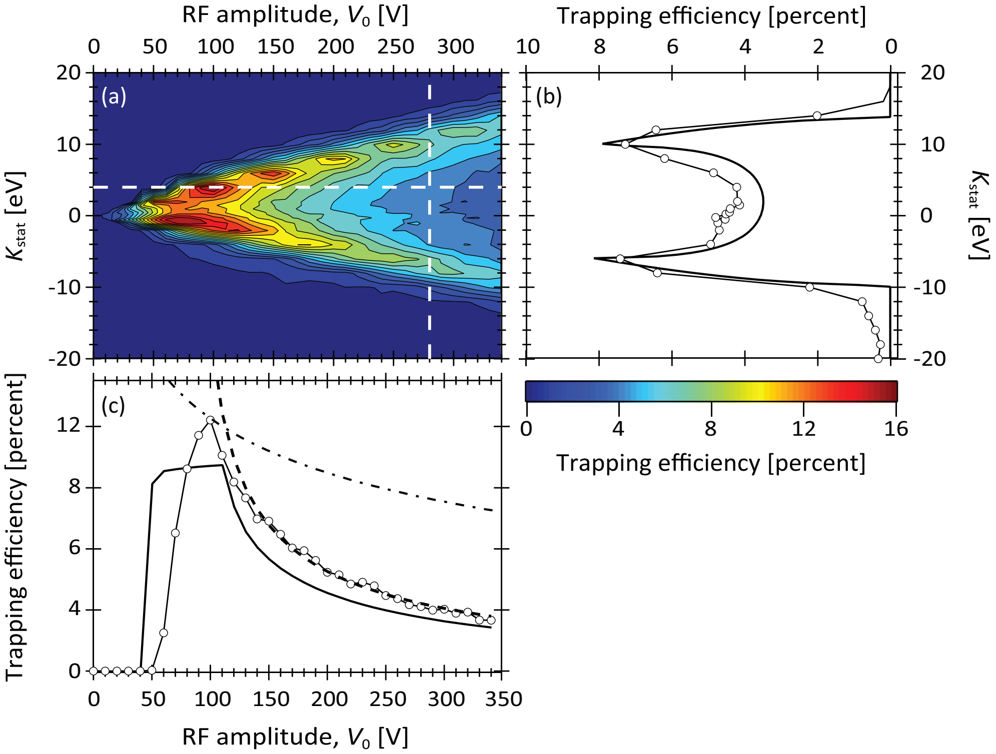

FIG. 8. (Color online) The simulated trapping efficiency in comparison to the analytical model. (a) Simulated trapping efficiency as a function of the nominal kinetic energy and the RF amplitude. The dashed lines mark the positions of the cross-sectional plots shown below and to the right. (b) Trapping efficiency as a function of the nominal kinetic energy when the RF amplitude is fixed at 280 V. Open circles represent the simulated results and the line the analytical trapping efficiency. A scaling factor was used for the analytical trapping efficiency to match the simulated results. (c) Trapping efficiency as a function of the RF amplitude when the nominal kinetic energy is 4 eV. Open circles represent the simulated results and the line the analytical trapping efficiency. A scaling factor [the same as for (b)] was used for the analytical trapping efficiency to match the simulated results. The dashed line is the curve obtained from Eq. (35), while the dash-dotted line shows the scaling of the square of the effective trapping radius which represents the decreasing behavior of the trapping volume [see Fig. 2(c)].

where the simulated results (open circles) are plotted together with the analytical model (lines). Despite the approximations made, the analytical model clearly describes the essence of the simulated trapping dynamics. The decrease of the trapping efficiency for high RF amplitudes [Fig. 8(c)] in the present case is thus verified to arise from the decreasing phase interval over which ions exchange with the RF field the energy needed to become trapped. Consequently, the decreasing behavior is very well reproduced by Eq. (35), as illustrated by the dashed line in Fig. 8(c).

In conclusion, the simulations verify the result of the analytical model, namely that the trapping efficiency is determined by an interplay between the trap depth and the ability of the longitudinal RF field to bring the ion kinetic energy into the energy acceptance region of the trap. However, the trap depth only depends on the RF amplitude for low amplitudes, which effectively means that the trapping efficiency is largely governed by the energy exchange between the ions and the longitudinal field.

2. Properties of the trapped ions

The previous sections demonstrated how the longitudinal RF field controls the kinetic energy of the ion arriving at the trap center and thereby enables trapping. The significance for the energy distribution of trapped ions is illustrated in more detail in Fig. 9, which shows the simulated energy distribution of ions when first arriving at the trap center and the simulated energy distribution of the stored ions for two different RF amplitudes. As seen in Figs. 9(a) and 9(b), the longitudinal RF field induces an energy distribution at the trap center, and this distribution becomes wider with increasing RF amplitude. In order to be trapped, the simulations show that the ion energy must fall to the left of the dash-dotted line marked in the figure, and ideally, this cutoff energy should correspond to the trap depth. The maximum trap depth is controlled by $\eta_{\max}$ [Eq. (15)], which must be set to a value of 0.64 to obtain the best agreement between the simulated and analytical trapping efficiency, as stated earlier. As marked by the long-dashed line in Figs. 9(a) and 9(b), the trap depth in this case is 3.8 eV, which is close to the simulated energy cutoff. For the simulation in Fig. 9(a), the RF field is just strong enough to bring part of the energy distribution into the range that allows for trapping, and the time-averaged energy distribution during trapping in this case is depicted in Fig. 9(c). This distribution clearly peaks around approximately 2.4 eV as a result of the low-energy peak in the energy distribution at the trap center. When the RF amplitude is increased, the energy distribution at the trap center becomes wider, and the peak at low energies no longer appears as this class of ions does not have enough kinetic energy to

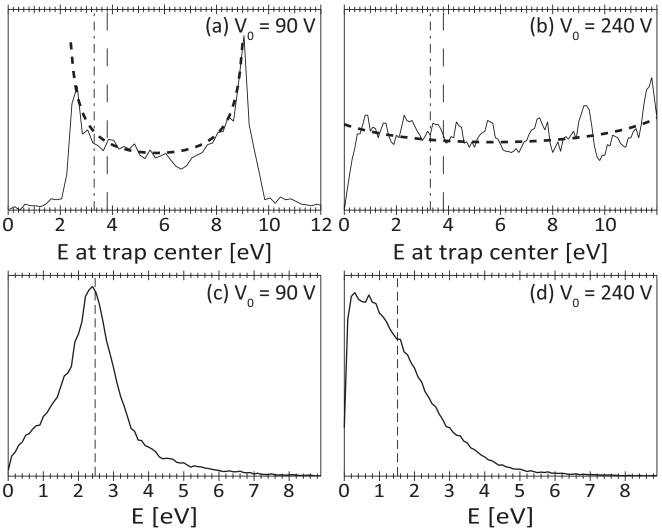

FIG. 9. The effect of the longitudinal RF field on the ion energy distribution. (a),(b) Simulated ion energy distribution when first arriving at the trap center for two different RF amplitudes. The region to the left of the dash-dotted line indicates the energy range of incoming ions that potentially can be trapped. For comparison, the trap depth corresponding to $\eta_{\rm max} = 0.64$ is shown as the long-dashed line. The short-dashed line represents the analytical energy distribution given by Eq. (37). (c),(d) Simulated instantaneous energy distribution of trapped ions for the two different RF amplitudes. The dashed line indicates the mean energy. In the simulations, the trap potential was set such that $K_{\rm stat} = 6$ eV.

reach the trap center [Fig. 9(b)]. The energy distribution in the energy range that leads to trapping is now essentially flat. Consequently, the instantaneous energy distribution of stored ions shown in Fig. 9(d) is peaked at lower energies, implying that more low-energy trajectories are populated. Note that the energy distributions in both cases have a tail that extends beyond the trap depth of 3.8 eV. Within the adiabatic model, the maximum transverse energy, $E_{\rm m}$, stored in the drift motion must be smaller than the trap depth for the ion to be stored, but the *instantaneous* kinetic energy, that is, the sum of the kinetic energy stored in the drift motion and micromotion, which is the quantity plotted in Figs. 9(c) and 9(d), is oscillating between 0 and roughly $3E_{\rm m}$ [19].

The observation of the peaks at high and low energies in the energy distribution at the trap center can, in fact, be rationalized from Eq. (30). In the simulations, ions enter the trap at times evenly distributed over the entire phase of the RF field, meaning that ϕ_0 is uniformly distributed on the interval $[0,2\pi)$, corresponding to a distribution function of $f(\phi_0) = 1/2\pi$. The distribution of the energy change at the trap center, $f(\Delta K_{\rm RF})$ can now be derived by requiring conservation of probability, $f(\Delta K_{\rm RF})d\Delta K_{\rm RF} = f(\phi_0)d\phi_0$, with the result

$$\begin{aligned} f(\Delta K_{\rm RF}) &= f(\phi_0)\frac{d\phi_0}{d(\Delta K_{\rm RF})} \propto \frac{d}{d(\Delta K_{\rm RF})}\arccos\frac{-\Delta K_{\rm RF}}{qeV_0T'_{\rm eff}} \\ &= \frac{1}{\sqrt{(qeV_0T'_{\rm eff})^2 - \Delta K_{\rm RF}^2}}. \end{aligned} \tag{37}$$

This expression is plotted in Figs. 9(a) and 9(b) as the dashed line, and it represents well the energy distribution thereby explaining the origin of the peaks. The above equation predicts that as the RF amplitude is increased, the energy distribution at the trap center becomes wider and quite flat in a large central region. Therefore, the energy distribution in the energy window for trapping will look the same for all RF amplitudes above a certain limit. Consequently, the ion energy distribution during storage converges towards some fixed distribution for high RF amplitudes.

In summary, the longitudinal RF field determines the energy distribution of the stored ions. As a consequence, also ions of low kinetic energies become trapped even without the use of buffer gas since a class of ions is effectively exchanging energy with the field thereby entering the trap with low kinetic energy.

V. INSTRUMENTATION

Figure 10 shows the layout of a newly realized experimental setup that can be used to investigate the injection and trapping of ions in a ring electrode trap. The apparatus consists of an accelerator equipped with an ion source, a 90° bending magnet for mass analysis, a transfer beamline, a RF ion trap situated on a high-voltage platform, and finally an MCP detector with a phosphor screen for ion detection. On the accelerator, which is of the isotope separator type [35], various ion sources can be mounted, thereby allowing for the production of a large range of ions. The transfer beamline comprises several electrostatic quadrupoles for focusing and deflectors for steering ions towards the central part of the setup, namely the ion trap which is followed by an MCP detector for ion detection.

The remainder of this section describes the details of the ion trap, the high-voltage platform, and the experimental procedure and can be skipped without loss of understanding of the results presented afterwards.

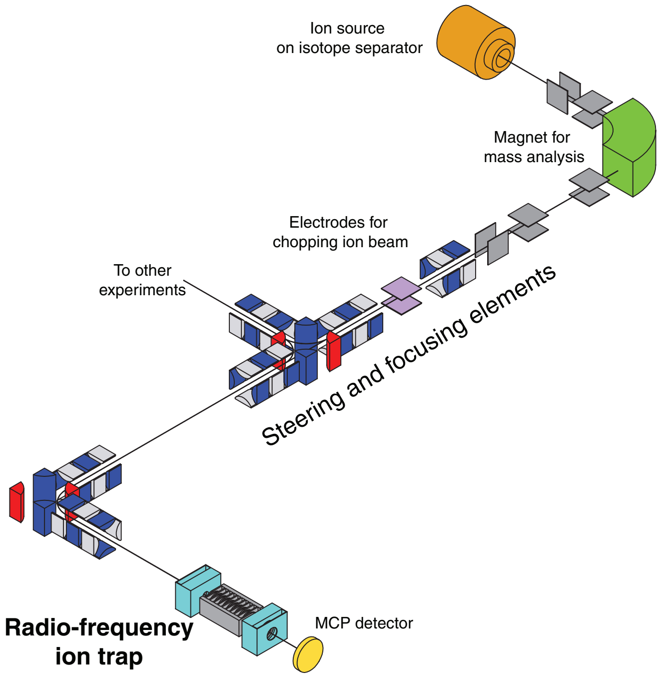

FIG. 10. (Color online) Schematic overview of the experimental setup.

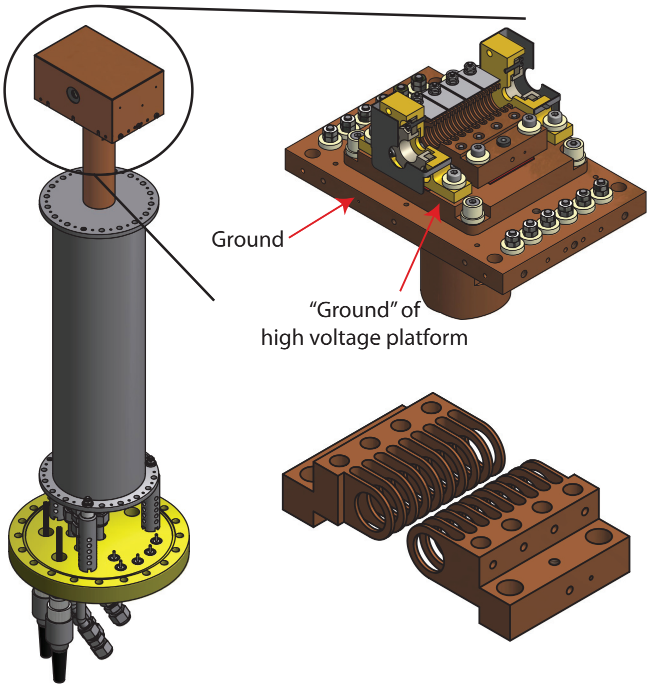

FIG. 11. (Color online) Views of the realized ring electrode trap. (Left) The trap mounted on the liquid nitrogen tank. (Right) Closeup of the trap assembly and the ring electrode arrangement.

A. Mechanical setup of the ring electrode trap

The mechanical construction of the RF ion trap is shown in Fig. 11. The design of the ring electrode trap is based on that of Gerlich and co-workers [36]. It consists of a stack of 20 1-mm-thick ring electrodes spaced by 1 mm ($2\pi z_0 = 4$ mm) and with an inner radius of $r_0 = 5$ mm (see Fig. 1). The electrode structure is machined out of two solid blocks of copper such that every second electrode belongs to the same block as depicted in Fig. 11. The end electrode assemblies consist of a copper block which acts as an electrode and also supports two other electrodes. The three electrodes all have a hole of varying inner diameter (6, 10, and 10 mm going outwards from the trap center) and depth (2, 6, and 1 mm, respectively) centered on the trap axis, thereby allowing ions to enter and exit the trap. The outer two electrodes (end caps) of this assembly are electrically connected, whereas the potential of the middle electrode (lens) is controlled independently. With this configuration, ions are focused into the trap, and by transiently changing only the potentials of the end caps, ions can be loaded into and extracted from the trap. Furthermore, the trap is equipped with four pairs of 9-mm-wide rectangular electrodes spaced by 1 mm placed just above and below the ring electrodes, and these make it possible to shape the potential along the trap axis and thereby manipulate the ion cloud (not exploited in this study). The ring and end electrode assemblies are mounted on a copper base plate from which they are electrically insulated by 0.5-mm-thick sapphire plates. The entire assembly comprising the base plate, ring electrode, and end electrode assemblies is kept at high potential relative to ground to achieve ion deceleration. The high-voltage platform that supplies the potentials to the trap is described in Sec. V B.

The baseplate assembly is mounted onto a second copper plate, which in turn is mounted onto a thick copper rod. To be able to cool the trap, this rod is immersed into a reservoir that can be filled with liquid nitrogen. The reservoir and the second copper plate are on ground potential, and the baseplate assembly is therefore electrically insulated from the second plate by a 0.5-mm-thick sapphire plate. Also attached to this second copper plate is a copper housing which surrounds the trap and which serves a double purpose. First, it screens the high trap potentials such that ions are only affected by these potentials when they are close to the trap entrance. Second, the cover separates the trap volume from the volume of the surrounding chamber. This is convenient if a reactant gas or a He buffer gas is introduced into the trap volume as the copper housing then allows for a high neutral-gas density within the trap volume, while a relatively low pressure is maintained in the surrounding vacuum chamber. Gas can be supplied to the trap via a central hole in the copper rod both of which go all the way through the reservoir.

The tank is mounted on a vacuum flange which carries electrical feedthroughs for all the trap potentials and feedthroughs for running liquid nitrogen through the reservoir and for letting either He buffer gas or a reactant gas into the trap volume.

The trap region is evacuated by a turbomolecular pump which, without gas load from the trap, maintains a background pressure of about 10^{-9} mbar in the surrounding chamber.

B. High-voltage platform

A schematic of the trap high-voltage (HV) platform is shown in Fig. 12. All electronics mounted in the HV cage are powered by a 500-W isolation transformer. Line power to the transformer itself is supplied through an interlock switch which disables the platform power if the door to the cage is opened or if the pressure in the chamber is too high. The platform potential is supplied by a 10-kV power supply (Spellman MPS Series) with a stability better than 0.02% per 8 h. The output terminal of this supply is connected to ground while its own ground terminal is connected to the secondary windings of the transformer. In this configuration, the power supply itself is residing in the HV cage and must be of positive polarity to keep the platform potential negative with respect to ground. This arrangement is prepared to keep together all trap-related power supplies and the communication to these. The potentials applied to the trap end caps, lenses, and grids are delivered by separate unipolar power supplies (Spellman MPS series) with voltage ranges ±500 V (end caps), ±1000 V (lenses), and ±1500 V (grids). To trap and eject ions, the potentials of the end electrodes and the lenses can be switched between two static outputs from the aforementioned supplies. The switches are home-built metal-oxide-semiconductor field-effect transistor switches in push-pull configuration, and switching is achieved in less than 100 ns. The RF signals for the trap ring electrodes are generated by a homemade 4-MHz RF supply capable of delivering a maximum peak-to-peak (p-p) amplitude of 1400 V. Communication between the control system and the electronics in the HV cage is provided by two optical links. One link is used for communication with a Beckhoff lightbus system which is equipped with digital-to-analog converters

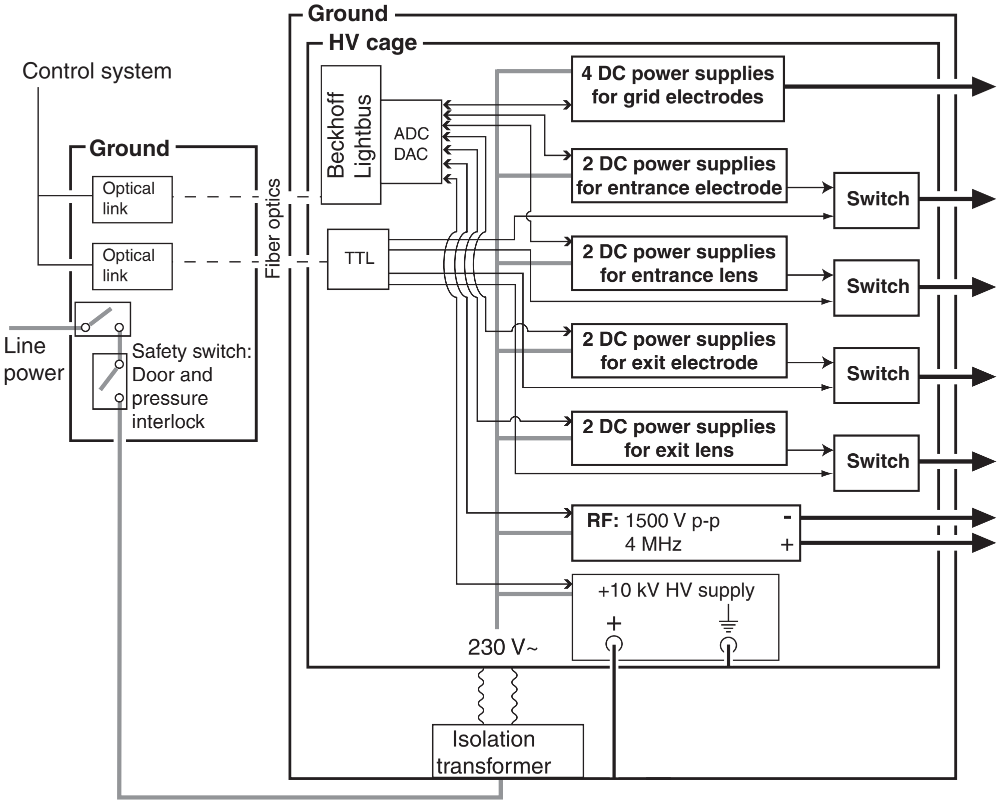

FIG. 12. Layout of the trap high-voltage platform.

and analog-to-digital converters for analog programming and monitoring of all power supplies residing in the cage. The other optical link is a fast TTL link used to deliver the different timing signals to the switches controlling the loading and extraction of ions. All signals are exiting the platform through coaxial cables with grounded shields such that the vacuum system itself can be kept at ground potential.

C. Experimental procedure

For the experiments presented here, a sputter ion source [37] is employed. Negative ions of charge $-|q|e$ are formed on the surface of a sputtering cathode consisting of silicon and are subsequently accelerated towards the source exit from the cathode kept at -2 kV relative to the front of the accelerator. Ions enter an acceleration tube with an energy of $2|q|$ keV, and as the front of the accelerator and the entire ion source are kept at -1 kV relative to ground, the ions acquire $1|q|$ keV of additional energy on their way through the acceleration tube, resulting in a total beam energy of $3|q|$ keV. After mass-to-charge selection in the bending magnet, a continuous current of 0.5 nA of $\mathrm{Si}_2{}^-$ is achieved. Further downstream, a set of fast-switched electrostatic deflectors (the ion chopper) is used to create a pulsed ion beam by letting the ions pass during a time span of 100 μs before the chopper potential is switched to a high level to block the beam. To achieve trapping initially, the trap HV platform is kept at ground potential while the pulsed ion beam is steered through the trap and imaged on the phosphor screen of the MCP detector located behind the trap. The potential of the trap platform is then slowly changed so as to decelerate the ions to energies of only a few eV, and typically the steering and focusing of the ions into the trap must be adjusted accordingly. At this point, ion trapping is achieved by applying appropriate potentials to the end electrodes at the trap entrance and exit. At first, the potential of the entrance electrode is set to focus ions into the trap while the potential applied to the exit electrode prevents ions from exiting the trap. When the last ions arrive at the trap, the potential of the entrance electrode is switched, and ions are now stored. After a variable storage time, the potential of the exit electrode is transiently lowered, and ions are extracted from the trap and detected at the MCP detector. The timing of the trap electrodes is synchronized with the timing of the ion chopper plates, and the former has a period of 51 ms in most experiments presented here. However, the ion chopper timing is running at a frequency which is only half of that of the trap timing so that data are acquired with and without ions alternatingly, thereby allowing for subtraction of background events.

VI. EXPERIMENTAL INVESTIGATIONS

The theory presented in Sec. III and the numerical simulations presented in Sec. IV A give rise to two main predictions that can be investigated experimentally. First, the validity of the injection mechanism that uses explicitly the longitudinal component of the RF field can be illustrated by observing ion trapping and investigating the trapping stability and efficiency in dependence of the RF amplitude and the nominal kinetic energy. Second, the proposed mechanism leads to ensembles of trapped ions with a characteristic energy distribution (see

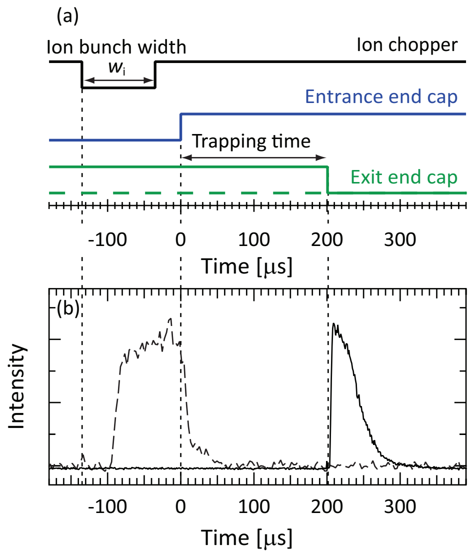

FIG. 13. (Color online) Operation of trap potentials and the corresponding ion time-of-flight (TOF) spectra. (Top) Timing sequence of the ion chopper and the trap entrance and exit end-cap electrodes. The high level of each trace corresponds to a potential which blocks ion passage. The green dashed line represents the operation of the exit end cap electrode in the case where ions are guided through the trap. (Bottom) Number of events recorded by the MCP detector as a function of time. Time zero is chosen to be the time at which the potential of the entrance electrode is switched to trapping mode. The dashed line shows the ion time-of-flight (TOF) spectrum when the exit electrode is statically set to transmission (guiding) (dashed green line below) while the solid line represents the TOF spectrum when the exit electrode initially is set to trapping and then later switched to transmission.

Fig. 9) which is illustrated by examining the ion decay from the trap and the dependence of the trapping efficiency on the end-cap potential.

A. Ion injection and extraction

Figure 13(a) summarizes schematically the operation of the RF trap electrode potentials during injection and extraction of ions. Figure 13(b) shows the synchronized ion signal recorded with the MCP detector. Two modes are indicated for the operation of the exit end-cap electrode. In guiding mode, the first particles arrive at the detector approximately 40 μs after the ions have passed the chopper electrodes. Particles continue to arrive for $\sim$100 μs corresponding to the time span during which the chopper allows ions to pass. In trapping mode, a potential is applied to the exit end-cap electrode to reflect the incoming ions, and when the last ions of the bunch arrive at the trap, also the potential of the entrance end-cap electrode is switched to repel ions and prevent them from leaving the trap. In the situation illustrated in Fig. 13, ions are extracted after a storage time of 200 μs and arrive at the detector during a time span of approximately 100 μs. The fact that it takes some ions 100 μs to leave the trap either implies that these ions are stored with low kinetic energies (a round-trip time of 100 μs corresponds roughly to a longitudinal kinetic energy of 0.25 eV) or that they make a couple of round trips before exiting the trap.

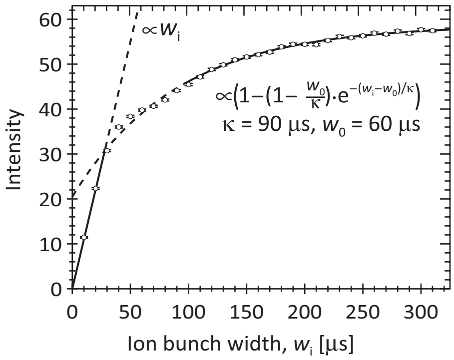

FIG. 14. Loading of ions into the RF trap. The open circles represent the measured intensity of ions released after 15 ms of trapping recorded as a function of the ion bunch width. The solid lines show the asymptotical behavior for short and long time scales, while the dashed lines illustrate the continuations of these functions outside their range of validity.

To investigate over which time span the trap can be loaded, the number of ions released after a trapping time of 15 ms was recorded as a function of the temporal width, w_i, of the injected ion bunch. The continuous ion beam delivered by the ion source is pulsed only by the chopper electrodes, and hence the number of ions reaching the trap is directly proportional to the ion bunch width determined by the pulsing of the chopper electrodes. Figure 14 shows the resulting intensity of extracted ions as a function of the ion bunch width. The number of trapped ions increases linearly with the chopper width for $w_i \lesssim 30$ μs, whereafter it increases slower to an almost constant level at $w_i \gtrsim 300$ μs. Consequently, ion trapping is most efficient during $\sim$30 μs where the number of stored ions increases linearly with the bunch width. The deviation from linearity above 30 μs could intuitively be attributed to space charge effects, but in the present case only some hundreds of ions are detected per trap cycle, implying that another explanation must be sought. During loading of the trap, there is no potential barrier that prevents ions from leaving the trap again through the entrance, and this situation naturally introduces loss of ions during injection. Hence, the linear increase in ion intensity with ion bunch width cannot continue indefinitely but will cease once the first injected ions begin to reach the entrance again. In a simplified model, the number of ions, N, that are present in the trap during injection and that have the potential of being trapped, is found by solving the differential equation,

$$\frac{dN}{dw_i} = n_0 - N/\kappa, \quad \text{for } w_i > w_0, \tag{38}$$

where n_0 is the rate of ions entering the trap, N/κ the rate of ions escaping from the trap, and w_0 the time at which ion loss through the entrance sets in. The solution to this differential equation is

$$N(w_i) = n_0\kappa\left[1 - \left(1 - \frac{w_0}{\kappa}\right)e^{-(w_i-w_0)/\kappa}\right], \quad w_i > w_0. \tag{39}$$

Thus, on the time scale where the loss of ions through the entrance becomes important, the observed ion intensity is expected to change from a linear dependence on w_i to the

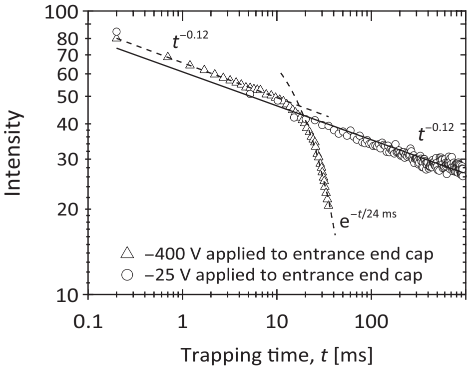

FIG. 15. Ion stability in the RF trap under different conditions of trapping. The curves show the intensity of extracted ions as a function of trapping time at an RF amplitude of 110 V. The curve with open circles was recorded when the entrance end cap was switched to −25 V in trapping mode, whereas the curve represented by open triangles was recorded when this same electrode was switched to −400 V. The solid line represents the best fit of a power law ($I \propto t^{-0.12}$) to the data represented by the open circles, whereas the dashed lines show the best fits to the data represented by the open triangles by a power law on a short time scale and an exponential decay on a longer time scale.

exponential dependence described by Eq. (39). The solid line in Fig. 14 $w_{\mathrm{i}} > 100\ \mu$s represents the best match of this model to the data in this region, yielding $\kappa = 90\ \mu$s and $w_0 = 60\ \mu$s. These two time scales for ion loss through the entrance are in good correspondence with the 100-μs time span over which ions are detected when extracted from the trap (see Fig. 13). The loss rate is fairly low despite the absence of a potential barrier at the entrance which is most likely due to the effective deceleration of a class of ions that are then moving in the trap with low kinetic energy.

B. Trapping stability

To characterize the stability of the RF trap, the number of ions remaining in the trap was measured as a function of trapping time for two different potentials applied to the entrance end cap in trapping mode as shown in Fig. 15. In the case of switching on the more shallow axial potential well (open circles), the ion signal exhibits a time dependence well represented by a power law, that is $I \propto t^{-n}$, where $n = 0.12$. In contrast, when switching to a steep repulsive potential on the entrance end cap (open triangles), the decay initially still resembles the power-law decay observed for the first setting, whereas the decay on a longer time scale approaches exponential behavior ($I \propto e^{-t/\tau}$, where $\tau = 24$ ms).

To interpret these observations it is first noted that ions are most likely lost from the trap by escaping over the radial potential barrier [Eqs. (13) and (15)], which is only a few eV [see Fig. 2(d)]. Loss of ions from the trap due to electron detachment by blackbody radiation at 300 K can be ruled out on account of the high vertical detachment energy of $\mathrm{Si}_2{}^-$, which is 2.23 eV [38]. Likewise, electron detachment through collisions with residual gas is negligible on the time scale studied here due to the low background pressure of 10^{-8} mbar and the relatively high detachment energy [38].

The power-law decay observed for the shallow axial well (open circles in Fig. 15) can be understood by considering the inhomogeneous nature of the injected ensemble of ions. As a consequence of the energy exchange with the RF field, injection of even a monoenergetic beam results in trapped ions with a significant energy spread, as seen in simulations (Fig. 9), and this leads to an occupation of both stable and quasistable orbits depending on the ion energy relative to the trap depth [Eqs. (13) and (15)]. The ensemble of ions then decays with decay times characteristic of the energy of the trapped ion, and hence the total observed decay obeys a power law stemming from a sum over many exponential decays.

The reason for the observed exponential decay when switching to a high repulsive potential on the end cap (open triangles in Fig. 15) is that the ion motion inside the trap is excited by the larger transient field present during the switching which is sufficient to render the trajectories unstable.

C. Trapping efficiency

The influence of the RF amplitude, V_0, and the platform potential, V_{trap}, on the number of trapped ions was studied. Ideally, the sought quantity is rather the trapping efficiency, i.e., the ratio of the number of trapped ions to the number of incoming ions, but this parameter is not easily quantified as the number of ions reaching the trap entrance when ion trapping is also applied cannot be recorded during these measurements. Hence, the quantity obtained in experiments is only proportional to the trapping efficiency. In order to compare the experimental results with the simulated results in Fig. 8, the trap-platform potential must be related to the nominal kinetic energy, K_{stat}, of the ions through Eq. (19). In this equation, the ion beam energy, K_0, can be approximated by the ion charge times the sputter potential, V_{sputter}, from which the ions are initially accelerated, yielding $K_{\mathrm{stat}} = -e(V_{\mathrm{sputter}} - V_{\mathrm{trap}})$. However, the ions might be emitted from the cathode with some energy [39,40] that is added to the energy acquired during the acceleration stage, and hence some uncertainty in the mean total ion beam energy, K_0, is expected. The zero point of the experimental K_{stat} scale in Fig. 16 is therefore chosen such that the best agreement between simulations and experiments is obtained, implying that an offset must be added to $-eV_{\mathrm{sputter}}$ to obtain the true ion beam energy. Figure 16(b) shows the trapping efficiency for a fixed trap potential and thereby fixed ion nominal kinetic energy as a function of RF amplitude, while Fig. 16(c) displays the trapping efficiency as a function of nominal kinetic energy for a fixed RF amplitude. The overall agreement between simulations and experiments is very good when considering that only an offset in the experimental K_{stat} scale and an overall scaling of the trapping efficiency is applied in the comparison. The fact that the simulations to a high degree reproduce the experimental results verifies that the loading dynamics is governed by the energy exchange between ions and the longitudinal RF field as suggested by the simulations and the analytical model. However, the experimental features are more blurred than those obtained from simulations. This deviation is most likely due to the finite energy spread of the ion beam which is less than 10 eV (FWHM) [37], and this spread is not accounted for by the simulations which employed a monoenergetic ion beam.

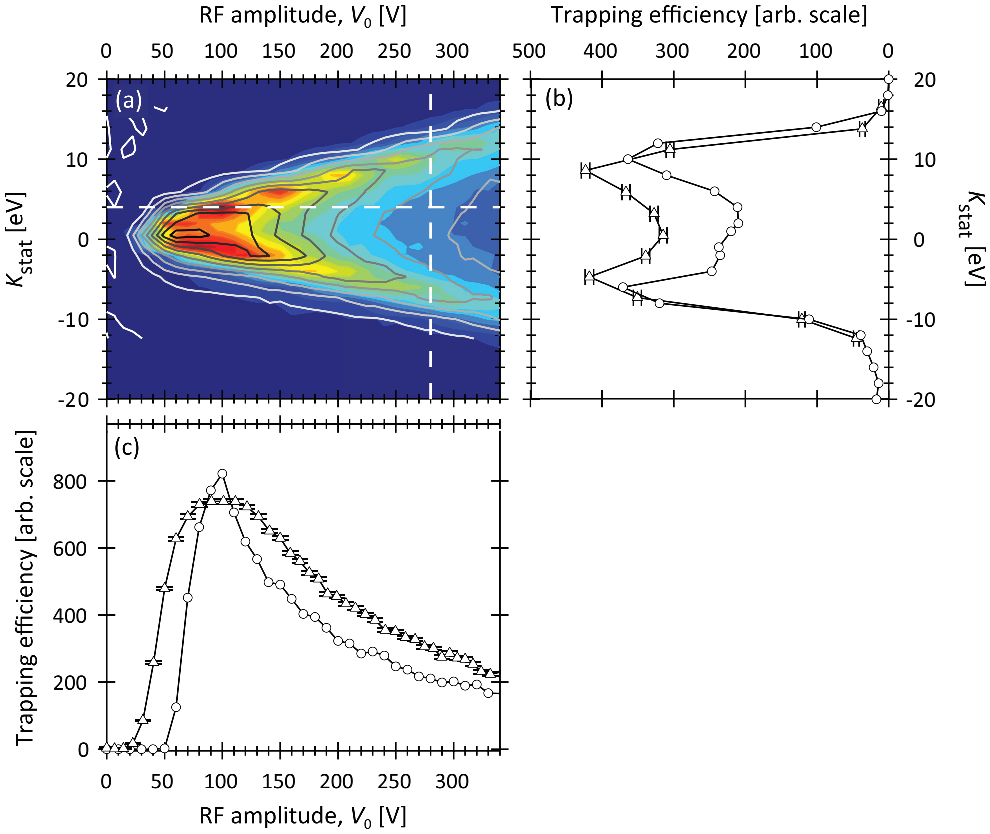

FIG. 16. (Color online) The trapping efficiency obtained from experiments in comparison to the simulated efficiency. (a) Comparison of experimental and simulated trapping efficiency as a function of the nominal kinetic energy and the RF amplitude. The colored contour plot represents the simulated trapping efficiency, and the experimental data are plotted on top as gray-scale contour lines. The dashed lines mark the positions of the cross sectional plots shown below and to the right. (b) Trapping efficiency as a function of the nominal kinetic energy when the RF amplitude is fixed at 280 V. Open triangles show the experimental results and open circles the simulated results. (c) Trapping efficiency as a function of the RF amplitude. Open triangles show the experimental results and open circles the simulated results when the nominal kinetic energy is 4 eV.

D. Energy distribution of injected ions

The energy distribution of the injected ions at different RF amplitudes was investigated by measuring the fraction of ions remaining in the trap as the repulsive potential applied to the entrance end cap during the entire trapping period was lowered. For a fixed nominal kinetic energy of ~0.5 eV [$= K_0 - qeV_{\text{trap}}$, Eq. (19)], Fig. 17(a) displays the results of such a measurement. To extract information on the ion energy distribution, the depth of the axial potential well must be determined since this depth, rather than the end-cap potential, sets the upper bound on the kinetic energy of ions that remain trapped. The end caps used to create the axial well have an opening diameter of 6 mm, and hence, on an absolute scale, the electric potential close to the trap axis arising from the end caps is lower than that applied to these electrodes. The axial well depth therefore exhibits a minimum at the trap axis, and simulations using the SIMION software were performed to determine how this minimum depth relates to the potential applied to the end cap. The ion fraction remaining in the trap can then be displayed as a function of the axial well depth as done in Fig. 17(a), where the bottom scale indicates the axial well depth. To obtain more quantitative information on the ion kinetic energy distributions, the distribution at a given RF amplitude was assumed to be Gaussian with mean energy E_0 and spread σ. The quantity probed experimentally is the cumulative distribution, which is then given by

$$P(E \leqslant U_{\text{ax}}) = \frac{1}{\sqrt{2\pi\sigma^2}} \int_{-\infty}^{U_{\text{ax}}} e^{-(E'-E_0)^2/2\sigma^2} dE'. \qquad (40)$$

Figure 17(b) displays the measured cumulative distribution obtained at two different RF amplitudes (solid circles and open triangles) together with the cumulative Gaussian distributions [Eq. (40)] that provide the best description of the data (solid and dashed lines). As seen, the Gaussian distributions give a fair representation of the data. Figure 17(c) shows the mean energy, E_0, as a function of RF amplitude (solid circles) while the width of the distribution is indicated by the dashed lines representing $E_0 \pm \sigma$. The results show that when the RF amplitude is increased initially, the mean energy and spread increase. This behavior is attributed to the increasing trap depth for small RF amplitudes, which enables trapping of ions with higher energies. At higher RF amplitudes, the mean energy and spread are decreasing again. This effect can be understood in terms of the energy distributions shown in Fig. 9. At low RF amplitudes where ion trapping for a given nominal kinetic energy is just becoming possible the energy distribution of the

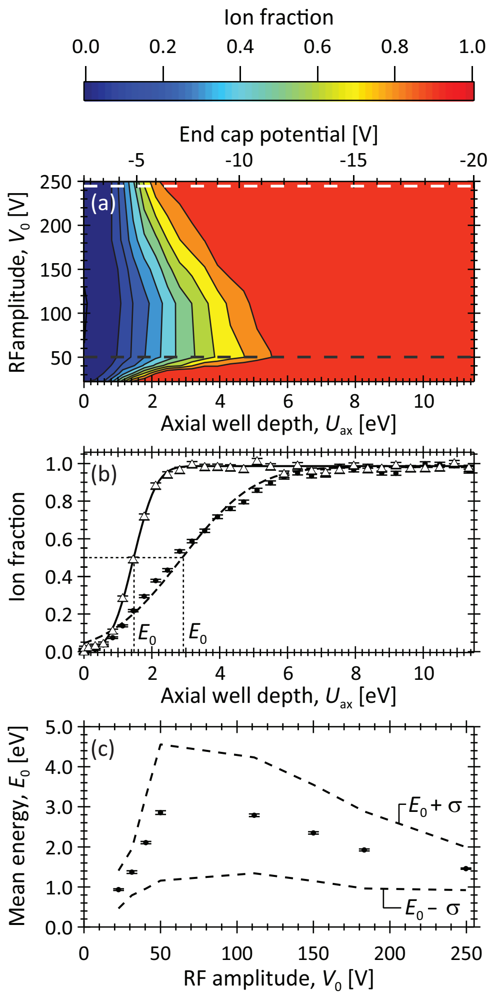

FIG. 17. (Color online) Energy distribution of injected ions. (a) Fraction of ions remaining in the trap as the trapping potential applied to the entrance electrode is lowered. The results for several RF amplitudes are shown. The dashed lines indicate the RF amplitudes at which the cross-sectional plots in (b) are shown. (b) Fraction of ions stored in the trap as a function of the trapping potential applied to the entrance electrode recorded at two different values of the RF amplitude. The data represented by the solid circles and the open triangles are recorded at RF amplitudes of 50 and 250 V as indicated by the black-and-white dashed lines in (a), respectively. The solid and dashed curves represent the cumulative Gaussian distribution functions that best describe the measurements represented by the solid circles and open triangles, respectively. (c) The mean value, E_0 (solid circles), and the mean value plus or minus the spread, σ (dashed lines), of the cumulative Gaussian energy distribution functions that best describe the measurements for each value of the RF amplitude. All of the presented data were recorded at a trap-platform potential where $K_{\mathrm{stat}} \approx 0.5$ eV.

stored ions is peaked around some nonzero value as illustrated in Fig. 9(c). In this case, the cumulative distribution levels off only at some high energy and correspondingly a higher blocking potential must be applied to the end electrode to retain most ions in the trap. As the RF amplitude is increased, Fig. 9(d) demonstrates that the energy distribution is now rather peaked at low energies. In this situation, the cumulative distribution reaches a high level at lower energies, implying that now a lower potential on the end electrode is needed to retain the same fraction of ions. Hence, the behavior of the experimental data presented in Fig. 17 can be explained by the energy distribution of the stored ions obtained in the simulations.

VII. DISCUSSION

The results presented above show that ions can be stored in an RF trap for seconds without the use of buffer gas to dissipate kinetic energy and that the decay of the number of ions remaining in the trap follows a power law. This behavior is attributed to the inhomogeneous nature of the injected ensemble of ions that exhibits a distribution of decay times. The observation is very similar to what has been observed for fast beams in electrostatic storage devices [41,42]. Power-law decays are also frequently encountered, for example, in the unimolecular statistical decay of an ensemble of isolated clusters or molecules that have a broad internal energy distribution [43]. Quite generally, such a nonexponential or power-law decay emerges whenever the decay of some system is described by a multitude of different decay rates.

Both the simulations and the experimental investigations clearly demonstrate that the longitudinal RF field plays a significant role in the trapping of ions which enter the trap with kinetic energies of the order of 40 eV as formulated in Sec. III. The longitudinal field is able to decelerate ions and thereby dissipate kinetic energy leading to trapping of ions with low energies, even in the absence of buffer gas. In this regime, trapping occurs only at certain RF phases that depend on the kinetic energy of the incoming ions, and ions are trapped with a wide range of kinetic energies. Earlier simulations have also proposed that this mechanism is responsible for trapping ions injected into 3D quadrupole traps [44–46], where a strong dependence on the RF phase was also observed, but no attempts to describe the findings starting from the work-energy theorem were done.

A direct implication of the described injection mechanism is that at high RF amplitudes the trapping efficiency decreases with increasing RF amplitudes [see Figs. 8(c) and 16]. Similarly, the trapping efficiency has been observed to decrease for high RF amplitudes for octupole ion traps [47] where the observations were attributed to the diminished spatial region in which motional stability occurs. The effect of the smaller spatial region for high RF amplitudes is not significant here, as the trapping efficiency would then scale as $\hat{r}_{\mathrm{trap}}^2$, which is clearly not the case as demonstrated by the dash-dotted line in Fig. 8(c).

The injection mechanism implies that ions can be accelerated by the longitudinal RF field provided they traverse the trap entrance at the right RF phases. As a consequence, it should, in fact, be possible to accumulate ions in the trap though a static repulsive potential is applied to the entrance electrode at all times. If the ions approach the entrance at the right RF phases, the longitudinal RF field can “lift” them over the repulsive barrier, thereby allowing them to enter the trap and be stored. It would seem that the ion can then escape from the trap again by the same mechanism. However, for this to happen the ion must return to exactly the right place at the right time, and the probability for this event is low since ion motion can be considered randomized after entering the trap due to many "collisions" with the RF field. Using this strategy, ions could continuously be loaded into the trap, and the simulations show that such a loading scheme is indeed feasible. This possibility is to be explored experimentally in future studies.

To improve trapping efficiency in the present setup, a buffer gas can be introduced, and since several injected ions are moving along pseudostable trajectories, only a few collisions are needed to obtain stability. Hence, the buffer gas density can be kept significantly lower than with other loading schemes where buffer gas must dissipate the kinetic energy within one round trip in the trap. This requires the mean-free path to be less than the trap dimensions, resulting in typical He densities of 10^{13}–10^{15} cm^{-3}. On account of the lower buffer gas density, it might therefore be advantageous for some experiments to load the trap with the aid of the longitudinal RF field as described above. For example, this could be experiments involving XUV light where ionization of the He buffer gas would be disadvantageous, an effect that is suppressed at lower buffer gas pressures. Furthermore, collisional quenching which lowers the fluorescence or fragmentation yield of photoexcited ions inside the trap can be reduced by this approach, and finally, it might be possible to retain dynamical information about the fragmentation process by keeping collisional relaxation of the translational degrees of freedom at a minimum. For example, it could be imagined that the energy gained by kinetic energy release during fragmentation causes an ionic fragment to move into unstable regions of phase space and the kinetic energy release would then possibly be mapped into the effective loss rate of the ionic fragment.

It should be noted that the accelerating or decelerating effect of the longitudinal RF field is significant only at high injection velocities. If ions are injected gently into the trap, say with energies around 1 eV, the longitudinal RF field does not alter the ion energy significantly. The behavior of the transit-time factors in Eqs. (25) and (28) reveals that this is the case. When the ion velocity approaches zero, the cosine function under the integral varies rapidly with z, and therefore the integral vanishes in the limit where the oscillations occur on a much shorter length scale than that on which the electric field changes. Consequently, T'_{eff}, and therefore also the change in kinetic energy, is negligible for low velocities. In this regime, trapping occurs with almost unity efficiency provided the kinetic energy of the incoming ions does not exceed the trap depth, and in the absence of buffer gas, it is now crucial to adjust the trap platform potential such that ions enter with kinetic energies below the trap depth of approximately 1 eV.

VIII. CONCLUSION

An experimental setup involving a RF ion trap for trapping ions from a fast beam was presented, and the mechanism for loading fast ions into the trap without the use of buffer gas was studied in detail. A simple analytical model to describe the loading of ions was developed and validated by numerical simulations. These results indicate that energy exchange between the ions and the longitudinal RF field at the trap entrance plays the decisive role in the initial trapping of ions, and this hypothesis is further supported by the experimental investigations.

Presently, several routes involving the trap are being followed, both in terms of exploring fundamental properties of the trap and in terms of extending the system towards XUV photofragmentation studies of trapped ions.

ACKNOWLEDGMENTS

This work was supported by the Lundbeck Foundation, the Carlsberg Foundation and the Danish Natural Science Research Council (Grant No. 21-03-0330).

---

[1] W. Paul, O. Osberghaus, and E. Fischer, Forschungsber. Wirtsch.- Verkehrminist. Nordrhein-Westfalen **Nr. 415** (1958).

[2] M. Keller, B. Lange, K. Hayasaka, W. Lange, and H. Walther, Nature (London) **431**, 1075 (2004).

[3] A. B. Mundt, A. Kreuter, C. Becher, D. Leibfried, J. Eschner, F. Schmidt-Kaler, and R. Blatt, Phys. Rev. Lett. **89**, 103001 (2002).

[4] D. J. Wineland, Phys. Scr. T **137**, 014007 (2009).

[5] D. Gerlich, Phys. Scr. T **59**, 256 (1995).

[6] A. K. Hansen, M. A. Srensen, P. F. Staanum, and M. Drewsen, Angew. Chem., Int. Ed. **51**, 7960 (2012).

[7] R. Otto, J. Mikosch, S. Trippel, M. Weidemuller, and R. Wester, Phys. Rev. Lett. **101**, 063201 (2008).

[8] S. D. Ivanov, O. Asvany, A. Witt, E. Hugo, G. Mathias, B. Redlich, D. Marx, and S. Schlemmer, Nat. Chem. **2**, 298 (2010).

[9] B. Bellina, I. Compagnon, L. Joly, F. Albrieux, A. Allouche, F. Bertorelle, J. Lemoine, R. Antoine, and P. Dugourd, Int. J. Mass Spectrom. **297**, 36 (2010).

[10] T. R. Rizzo, J. A. Stearns, and O. V. Boyarkin, Int. Rev. Phys. Chem. **28**, 481 (2009).

[11] Q. Bian, M. W. Forbes, F. O. Talbot, and R. A. Jockusch, PhysChemChemPhys. **12**, 2590 (2010).

[12] K. Chingin, H. Chen, G. Gamez, and R. Zenobi, J. Am. Soc. Mass Spectrom. **20**, 1731 (2009).

[13] H. Kreckel *et al.*, Phys. Rev. Lett. **95**, 263201 (2005).

[14] S. B. Nielsen, A. Lapierre, J. U. Andersen, U. V. Pedersen, S. Tomita, and L. H. Andersen, Phys. Rev. Lett. **87**, 228102 (2001).

[15] F. Herfurth, J. Dilling, A. Kellerbauer, G. Bollen, S. Henry, H. Kluge, E. Lamour, D. Lunney, R. Moore, C. Scheidenberger, S. Schwarz, G. Sikler, and J. Szerypo, Nucl. Instrum. Methods Phys. Res., Sect. A **469**, 254 (2001).

[16] X.-B. Wang, H.-K. Woo, and L.-S. Wang, J. Chem. Phys. **123**, 051106 (2005).

[17] W. Paul, Rev. Mod. Phys. **62**, 531 (1990).

[18] R. E. March, J. Mass Spectrom. **32**, 351 (1997).

[19] D. Gerlich, in *State-Selected and State-to-State Ion-Molecule Reaction Dynamics. Part 1: Experiment*, Advances in Chemical Physics Series, Vol. LXXXII, edited by C.-Y. Ng and M. Baer (Wiley, New York, 1992), pp. 1–176.

[20] O. Asvany and S. Schlemmer, Int. J. Mass Spectrom. **279**, 147 (2009).

[21] E. Teloy and D. Gerlich, Chem. Phys. **4**, 417 (1974).

[22] R. E. March, Rapid Commun. Mass Spectrom. **12**, 1543 (1998).

[23] D. Gerlich, in *Molecules and Grains in Space*, edited by I. Nenner (AIP Press, New York, 1994), pp. 489–503.

[24] H. G. Dehmelt, Adv. At. Mol. Phys. **3**, 53 (1967).

[25] J. Mikosch, U. Fruhling, S. Trippel, R. Otto, P. Hlavenka, D. Schwalm, M. Weidemuller, and R. Wester, Phys. Rev. A **78**, 023402 (2008).

[26] Trapping of ion beams can be achieved with electrostatic fields only [27,28] as the field is changing in the rest frame of the ions.

[27] S. P. Møller, Nucl. Instrum. Methods Phys. Res., Sect. A **394**, 281 (1997).

[28] D. Zajfman, O. Heber, L. Vejby-Christensen, I. Ben-Itzhak, M. Rappaport, R. Fishman, and M. Dahan, Phys. Rev. A **55**, R1577 (1997).

[29] M. Weiss, in *Proceeding of CAS School: Fifth General Accelerator Physics Course*, edited by S. Turner (CERN, Meyrin, Switzerland, 1994), Vol. 94–01, pp. 913.

[30] E. A. Wadlinger, W. P. Lysenko, B. Rusnak, and K. Saadatmand, AIP Conf. Proc. **392**, 941 (1997).

[31] The equation is only valid in the quasielectrostatic limit where the frequency of the oscillating field is low enough that the wavelength is much greater than the geometrical dimensions as discussed by Friedman and co-workers [32].

[32] M. H. Friedman, A. L. Yergey, and J. E. Campana, J. Phys. E: Sci. Instrum. **15**, 53 (1982).

[33] For a given V_0, the ion velocity during the passage through the entrance RF field is considered to be a constant equal to the mean ion velocity, v_{ion}, during the traversal of the longitudinal field. In general, this constant depends on V_0 .

[34] SIMION 8.0, Scientific Instrument Services, Inc. Ringoes, NJ.

[35] K. O. Nielsen, in *Recent Developments in Mass Spectroscopy*, edited by K. Ogata and T. Hayakawa (University Park Press, Baltimore, 1970), p. 506.

[36] A. Luca, S. Schlemmer, I. Cermak, and D. Gerlich, Rev. Sci. Instrum. **72**, 2900 (2001).

[37] P. Tykesson, H. Andersen, and J. Heinemeier, IEEE Trans. Nucl. Sci. **23**, 1104 (1976).

[38] S. J. Peppernick, K. D. D. Gunaratne, S. G. Sayres, and A. W. Castleman, Jr., J. Chem. Phys. **132**, 044302 (2010).

[39] R. E. Honig, J. Appl. Phys. **29**, 549 (1958).

[40] H. Oechsner, Appl. Phys. **8**, 185 (1975).

[41] H. B. Pedersen, D. Strasser, O. Heber, M. L. Rappaport, and D. Zajfman, Phys. Rev. A **65**, 042703 (2002).

[42] L. Lammich, L. H. Andersen, G. Aravind, and H. B. Pedersen, Phys. Rev. A **80**, 023413 (2009).

[43] K. Hansen, J. U. Andersen, P. Hvelplund, S. P. Møller, U. V. Pedersen, and V. V. Petrunin, Phys. Rev. Lett. **87**, 123401 (2001).

[44] V. M. Doroshenko and R. J. Cotter, J. Mass Spectrom. **31**, 602 (1997).

[45] C.-S. O and H. A. Schuessler, J. Appl. Phys. **52**, 1157 (1981).

[46] S. T. Quarmby and R. A. Yost, Int. J. Mass Spectrom. **190-191**, 81 (1999).

[47] J. Walz, I. Siemers, M. Schubert, W. Neuhauser, R. Blatt, and E. Teloy, Phys. Rev. A **50**, 4122 (1994).